Monthly Notices of the ROYAL ASTRONOMICAL SOCIETY

MNRAS **543,** 2442–2462 (2025) https://doi.org/10.1093/mnras/staf1535
Advance Access publication 2025 September 16

BOWIE-ALIGN: weak spectral features in KELT-7b's *JWST* NIRSpec/G395H transmission spectrum imply a high cloud deck or a low-metallicity atmosphere

Eva-Maria Ahrer [1]★ Charlotte Fairman [2] James Kirk [3] Hannah R. Wakeford [2] Joanna K. Barstow [4] Anna B. T. Penzlin [3,5] Lili Alderson [6] Richard A. Booth [7] Duncan A. Christie [1] Alastair B. Claringbold,[8,9] Emma Esparza-Borges [10,11] Carlos Gascón [12] Mercedes López-Morales [13] N. J. Mayne [14] Mason McCormack [15] Annabella Meech [12] Paul Mollière [1] James E. Owen [3,16] Vatsal Panwar [8,9] Denis E. Sergeev [2] Daniel Valentine [2] Peter J. Wheatley [8,9] and Maria Zamyatina [14]

[1]*Max Planck Institute for Astronomy (MPIA), Königstuhl 17, D-69117 Heidelberg, Germany*
[2]*School of Physics, HH Wills Physics Laboratory, University of Bristol, Tyndall Avenue, Bristol BS8 1TL, UK*
[3]*Department of Physics, Imperial College London, London SW7 2AZ, UK*
[4]*School of Physical Sciences, The Open University, Milton Keynes MK7 6AA, UK*
[5]*Ludwig-Maximilians-Universität München, Universitäts-Sternwarte, Scheinerstr. 1, D-81679 München, Germany*
[6]*Department of Astronomy, Cornell University, 122 Sciences Drive, Ithaca, NY 14853, USA*
[7]*School of Physics and Astronomy, University of Leeds, Leeds LS2 9JT, UK*
[8]*Centre for Exoplanets and Habitability, University of Warwick, Gibbet Hill Road, Coventry CV4 7AL, UK*
[9]*Department of Physics, University of Warwick, Gibbet Hill Road, Coventry CV4 7AL, UK*
[10]*Instituto de Astrofísica de Canarias, C. Vía Láctea, San Cristóbal de La Laguna E-38205, Spain*
[11]*Department of Astrophysics, University of La Laguna, San Cristóbal de La Laguna E-38200, Spain*
[12]*Center for Astrophysics | Harvard & Smithsonian, 60 Garden St, Cambridge, MA 02138, USA*
[13]*Space Telescope Science Institute, 3700 San Martin Drive, Baltimore, MD 21218, USA*
[14]*Department of Physics and Astronomy, Faculty of Environment, Science and Economy, University of Exeter, Exeter EX4 4QL, UK*
[15]*Department of Astronomy & Astrophysics, University of Chicago, Chicago, IL 60637, USA*
[16]*Department of Earth, Planetary, and Space Sciences, University of California, Los Angeles, CA 90095, USA*

Accepted 2025 September 9. Received 2025 September 8; in original form 2025 June 25

ABSTRACT

Hot Jupiters and their atmospheres are prime targets for transmission spectroscopy due to their extended atmospheres and the corresponding large signal-to-noise, providing the best possible constraints for the atmospheric carbon-to-oxygen (C/O) ratio and metallicity of exoplanets. Within BOWIE-ALIGN, we aim to compare *JWST* spectra of a sample of orbitally aligned and misaligned hot Jupiters orbiting F-type stars to probe the link between hot Jupiter atmospheres and planet formation history. Here, we present a near-infrared transmission spectrum of the aligned planet KELT-7b using one transit observed with *JWST* NIRSpec/G395H. We find weak features, only tentative evidence for H_2O and CO_2 in the atmosphere of KELT-7b. This poses a challenge to constrain the atmospheric properties of KELT-7b and two possible scenarios emerge from equilibrium chemistry and free chemistry retrievals: a high-altitude cloud deck muting all features or an extremely low metallicity atmosphere, respectively. The retrieved C/O ratios from our data reductions range from 0.43–0.74, while the atmospheric metallicity is suggested to be solar to super-solar (1–16× solar). Although these wide constraints prevent detailed conclusions about KELT-7b's formation history, a solar-to-super-solar metallicity would imply the accretion of solid material during its formation, which is valuable information for the survey's wider goals of understanding the relative importance of gaseous to solid accretion.

Key words: exoplanets – planets and satellites: atmospheres – planets and satellites: gaseous planets – planets and satellites: individual: KELT-7b.

1 INTRODUCTION

One of the strongest motivations behind studying the atmospheres of hot Jupiters is the possibility of linking their present-day atmospheres to their formation and evolution. This led to the hypothesis that the formation location can be determined by the hot Jupiter's carbon-to-

★ E-mail: ahrer@mpia.de

© The Author(s) 2025.
Published by Oxford University Press on behalf of The Royal Astronomical Society. This is an Open Access article distributed under the terms of the Creative Commons Attribution License (https://creativecommons.org/licenses/by/4.0/), which permits unrestricted reuse, distribution, and reproduction in any medium, provided the original work is properly cited.

Downloaded from https://academic.oup.com/mnras/article/543/3/2442/8255897 by Imperial College London Library user on 04 November 2025

oxygen (C/O) ratio based on the ice lines in a protoplanetary disc, mostly motivated by Öberg, Murray-Clay & Bergin (2011). However, many mechanisms and processes have since been suggested that can also alter the atmospheric C/O ratio of a hot Jupiter beyond the equilibrium chemistry approach. This includes planetary migration (e.g. Madhusudhan, Amin & Kennedy 2014; Booth et al. 2017; Penzlin et al. 2024), disc ice lines evolving (e.g. Morbidelli et al. 2016; Owen 2020), and solids drifting within the disc (Booth et al. 2017; Schneider & Bitsch 2021). This is further complicated by the fact that models do not cover all the diversity found from observations of discs (Law et al. 2021), and the unknown relation between solid and gaseous accretion (e.g. Espinoza et al. 2017).

With this high number of unknown and unconstrained parameters, it remains challenging to use C/O ratios as tracers for planet formation locations (e.g. Mollière et al. 2022). However, Penzlin et al. (2024) demonstrated that the opportunity lies in numbers: that is, by observing a statistical sample of two populations that in theory should have formed or migrated differently resulting in different C/O ratios, we could constrain planet formation models. While models cannot predict quantitative values, they do robustly predict qualitative relative trends between populations; together with Kirk et al. (2024a), Penzlin et al. (2024) showed that C/O ratios and metallicities of hot Jupiters that have undergone disc migration should diverge from those that migrate after disc dispersal (disc-free or high-eccentricity migration) as disc-migrated planets accrete inner disc material (e.g. see also Madhusudhan et al. 2014; Booth et al. 2017).

Reliably and accurately measuring C/O ratios and metallicities in exoplanet atmospheres has proven challenging. For example, even when we can resolve both carbon- and oxygen-bearing species with *J WST*, we find that the retrieved values are influenced by retrieval set-up (e.g. Lueber et al. 2024; Welbanks et al., in preparation) and detector offsets (e.g. Ahrer et al. 2025). In addition, the limited range of atmospheric pressures probed with transmission spectroscopy might not be representative of the overall planetary composition (Dobbs-Dixon & Cowan 2017), and processes such as local atmospheric mixing (e.g. Zamyatina et al. 2024), cloud formation (e.g. Helling et al. 2016), or a planet's interior evolution (Müller & Helled 2024) might further alter the atmospheric composition we are observing. Therefore, further systematic observational studies are required to address these theoretical and observational obstacles.

Following these studies and challenges, our survey 'BOWIE-ALIGN' (*JWST* programme ID: GO 3838, PIs: Kirk & Ahrer) is set out to observe a sample of hot Jupiters, where half are in an aligned orbit, i.e. their orbital planes are perpendicular to the stellar axes meaning that they are aligned with the stellar equator; the other half of the sample is in a misaligned orbit around their host stars, i.e. exhibiting a significantly tilted orbital plane ($>45^\circ$ by our definition). The aligned hot Jupiters are presumed to have migrated through the disc, while the misaligned ones are expected to have undergone high-eccentricity migration after the disc has dispersed. We determined our sample based on their orbital (mis)alignment in addition to only considering hot Jupiters that orbit F stars above the Kraft break (effective temperatures $\gtrsim 6100$ K). These stars have radiative outer envelopes that result in inefficient tidal realignment (e.g. Albrecht et al. 2012), which reduces the possibility of our aligned sample falsely including initially misaligned planets (via high-eccentricity migration) that have had their obliquities damped.

In this work, we present the *JWST* NIRSpec/G395H observations of KELT-7 b, the third planet in our programme. For first planet, WASP-15b (misaligned), Kirk et al. (2025) found that its atmospheric metallicity is super-solar while its C/O ratio is consistent with solar, implying planetesimal accretion. Kirk et al. (2025) further reported evidence for the photochemical product SO_2 in the atmosphere of WASP-15b. Meech et al. (2025) found that the observations of the second planet, TrES-4b (aligned), suggest that its atmospheric C/O ratio and metallicity are subsolar. This points towards oxygen-rich gas accretion or to a combination of carbon-poor solid and low-metallicity gas accretion.

Table 1. Stellar and planetary parameters for the KELT-7 planetary system.

Parameter	Value	Ref.
Spectral type	F/F2	[1/2, 3]
Effective temperature, $T_{\rm eff}$ (K)	6768 ± 7	[4]
Age (Gyr)	1.3 ± 0.2	[1]
Surface gravity, log g [$\log_{10}$(cm/s^2)]	4.149 ± 0.019	[1]
Metallicity [Fe/H] (dex)	$0.139^{+0.075}_{-0.081}$	[1]
Stellar mass, M_* ($M_\odot$)	1.76 ± 0.25	[4]
Stellar radius, R_* ($R_\odot$)	$1.768^{+0.013}_{-0.029}$	[5,6]
Planetary mass, $M_{\rm p}$ ($M_{\rm Jup}$)	1.39 ± 0.22	[4]
Planetary radius, $R_{\rm p}$ ($R_{\rm Jup}$)	1.60 ± 0.06	[4]
Equ. temperature, $T_{\rm eq}$ (K)	2048 ± 27	[7]
Orbital period, P (days)	$2.7347703^{+0.0000037}_{-0.0000039}$	[8]
Obliquity, λ (degrees)	$-10.55 \pm 0.27^\circ$	[9]

Note. References are as follows: [1] Bieryla et al. (2015), [2, 3] Cannon & Pickering (1918, 1993), [4] Stassun et al. (2017), [5] Gaia Collaboration (Gaia DR3, 2023), [6] Andrae et al. (Gaia DR3 GSP-Phot, 2023), [7] Bieryla et al. (2015), [8] Patel & Espinoza (2022), and [9] Tabernero et al. (2022).

KELT-7 b was discovered by Bieryla et al. (2015) and has a mass of $1.39 \pm 0.22\,M_{\rm Jup}$ and a radius of $1.60 \pm 0.06\,R_{\rm Jup}$ (Stassun, Collins & Gaudi 2017). Its equilibrium temperature has been estimated as 2048 ± 27 K (Bieryla et al. 2015). With these planetary parameters, KELT-7 b is on the boundary of being a hot or ultra-hot Jupiter as combined with its surface gravity its dayside may reach temperatures where most molecules dissociate (Parmentier et al. 2018). The parameters of its host star, KELT-7, are summarized in Table 1. Based on its measured obliquity of $-10.55 \pm 0.27^\circ$ (Tabernero et al. 2022), KELT-7 b belongs to the aligned sample, i.e. the sample within the BOWIE-ALIGN survey to have migrated within their protoplanetary discs.

KELT-7 b's atmosphere has been studied previously. Pluriel et al. (2020) found evidence for H_2O in transmission and emission using the *Hubble Space Telescope* (*HST*) Wide Field Camera 3 (WFC3) G141 grism (1.1–1.7 μm). The same observations also suggested the presence of H^- absorption which was further confirmed by Changeat et al. (2022). Recently, Gascón et al. (2025) presented a new *HST* WFC3/UVIS (ultraviolet-visible) G280 featureless transmission spectrum covering 0.19–0.8 μm. In combination with the *HST* G141 data and the H^- absorption features, Gascón et al. (2025) also show evidence for water dissociation in their analysis. Under the assumption of thermochemical equilibrium, hot Jupiters with temperatures <2500 K may not exhibit strong H^- absorption features (Kitzmann & Heng 2018), though a combination of photochemical and collisional processes may lead to a higher production of H^- at temperatures <2500 K (Lewis et al. 2020), especially on hot Jupiters orbiting F stars with intense UV irradiation. The evidence of dissociation of H_2O in KELT-7 b's atmosphere may affect any abundance constraints of H_2O retrieved using *JWST* observations and thus influence the inferred C/O ratio and metallicity.

Other studies such as high-resolution atmospheric observations of KELT-7 b have not shown any significant detections of atomic species in the atmosphere. Tabernero et al. (2022) used HORuS

Downloaded from https://academic.oup.com/mnras/article/543/3/2442/8255897 by Imperial College London Library user on 04 November 2025

(the High Optical Resolution Spectrograph) mounted on the GTC (Gran Telescopio Canarias) to search for the presence of Hα, Li I, Na I, Mg I, and Ca II in KELT-7 b's atmosphere, but were only able to place upper limits on their abundances. Similarly, Sicilia et al. (2025) did not detect Na I features using TNG/HARPS-N observations.

This manuscript is structured as follows. First, we discuss the observations in Section 2, which is followed by the description of the data reduction and analysis in Section 3. Our atmospheric retrieval set-ups are laid out in Section 4, followed by the discussion of our results in Section 5 and our conclusions in Section 6.

2 OBSERVATIONS

Our *JWST* observations of KELT-7 b took place on 2024 February 3 using NIRSpec/G395H, NRSRAPID readout in the Bright Object Time Series mode. We used five groups/integrations, with 4976 total integrations and an overall observing time of 7.51 h, consisting of 2.35 h pre-transit, 3.51 h in-transit, and 1.66 h post-transit time. The data was split into four segments. After ingress, at around one third of the transit time (around BJD_MJD 60363.874, integration # 2365), we observed a jump in the data, suggesting that a mirror tilt event took place. We investigated this event further in Section 3.1.2. This mirror tilt event took place in a period where there was a resurgence of these events observed and only a few weeks prior to the largest seen event seen in the *JWST* science era[1] (Perrin et al. 2024).

3 DATA REDUCTION

To reduce our data, we used three independent pipelines:Eureka!, ExoTiC-JEDI, and Tiberius. This enabled us to check whether our resulting conclusions were independent of the method used to reduce the data and to fit the light curves with the tilt event. We describe the approaches used during the independent reductions in the following subsections, following standard reduction and analysis process routines with the exception of the additional fitting of the mirror tilt-event.

3.1 Eureka!

Eureka! is an open-source pipeline (Bell et al. 2022)[2] for the reduction of time-series observations with *JWST* as well as *HST*. It has been benchmarked against other pipelines and has been successfully used in multiple *JWST* data sets (e.g. Ahrer et al. 2023; Bell et al. 2023; Moran et al. 2023; Beatty et al. 2024; Kirk et al. 2025; Meech et al. 2025).

3.1.1 Light-curve extraction

We started our Eureka! analysis with the `uncal.fits` files. Eureka! Stages 1 and 2 are wrapped around the default JWSTpipeline (v1.12.2, context map 1242) steps. We followed the default steps (with a jump step threshold of 10σ) in addition to 1/f background subtraction at the group level and we opted for using a custom scale factor (using a smoothing filter calculated from the first group) for the bias correction.

In Stage 3 of Eureka!, we extract the time-series 1D spectra. We masked outliers greater than five times the median in the spatial direction and used double-iterative masking with $>5\sigma$ along the time axis. We correct for the curvature of the trace and subtract the background by fitting a constant for each frame to the area that is > 6 pixels away from the central pixel of the spectral trace. Within the JWST pipeline each integration receives a calibrated wavelength map from which we extract the wavelength at the source position. Finally, we perform optimal spectral extraction (Horne 1986) using a full width of 9 pixels. This is followed by Eureka!'s Stage 4, where we bin our data to the respective wavelength resolutions ($R = 100$ and $R = 400$) and clip outliers $>5\sigma$ based on a box car filter width of 20 pixels used to calculate a rolling median. We also generated a white light curves for NRS1 and NRS2.

3.1.2 Mirror tilt event

During our *JWST* observations of KELT-7 b, a mirror tilt event occurred, causing a change in the flux in our light curves. A tilt event is defined as an abrupt change in the position of a mirror segment that happens occasionally at varying magnitudes (e.g. see Rigby et al. 2023). This was also seen in previous transit observations, e.g. in HAT-P-14b (Schlawin et al. 2023) and WASP-39b (Alderson et al. 2023). Alderson et al. (2023) find that either fitting a simple step model or detrending the light curve using trace properties such as full width half-maximum (FWHM) or trace position worked equally well. In our ExoTiC-JEDI light-curve fitting, we test detrending against x and y position and while it accounted for some variations due to the tilt event, we required an additional step function to model the light curve adequately. We note that in contrast to the WASP-39b tilt event the effect was not clearly visible in the FWHM or positional tracers of our KELT-7 b observations. This is likely because the tilt event observed here is much smaller in magnitude and the data exhibits more noise, likely due to the smaller number of groups.

We investigated this event by looking at the *JWST* NIRISS Fine Guidance Sensor (FGS) data, which provides guide star imaging data in parallel to every *JWST* observation. For this purpose, we use the Python package SPELUNKER (Deal & Espinoza 2024), developed to enable access and provide useful tools to analyse these guide star data products. We fit a 2D Gaussian to extract the guide star flux and bin it to the time stamps of our transit. The time sampling of the FGS is at 64 ms per exposure, while the time between our integrations is 5.43 s. Then we compare the fitted width of the guide star (σ_x) to the NRS1 and NRS2 light curves, see Fig. 1. We find a definite jump in the guide star width, however, it does not exactly line up with the time of the event seen in the light curve. It is $\sim$5 mins apart, which we attribute to the fact that the FGS time stamps are not calibrated in the same way as the scientific observations are and can show offsets of that order [confirmed by private communication with N. Espinoza (STScI)]. This is further confirmed as the last time stamp from the FGS data is 3 min before the end of our observations (see also Fig. 1). Thus, while we try using this data for the detrending of the light curves at a later stage (with a time offset), it resulted in the same result as simply fitting a step function so we elected to use the latter, simpler method.

3.1.3 Light-curve fitting

We fit our extracted light curves using Eureka!'s Stage 5 using a BATMAN transit light-curve model (Kreidberg 2015) and a linear in

[1] *JWST* User Documentation; accessed 2025 August 5
[2] We used version v0.11.dev245+ge8ea1d1c.d20240701.

Downloaded from https://academic.oup.com/mnras/article/543/3/2442/8255897 by Imperial College London Library user on 04 November 2025

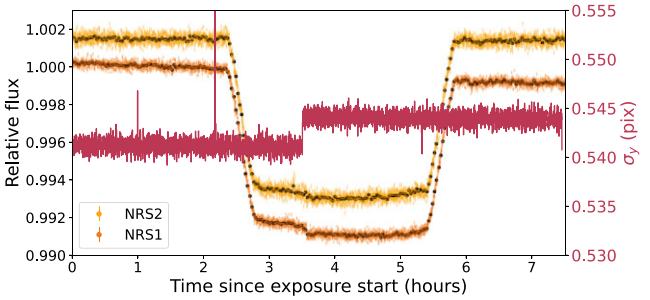


Figure 1. KELT-7 b transit white light curve of NRS2 (top) and NRS1 (second from the top) compared to one of the fitted widths (σ_x, dark line) to the *JWST* guidance data using the PYTHON package SPELUNKER (Deal & Espinoza 2024), binned to the time stamps of our light curve. We find that there is a definite tilt event visible in both. However, the time stamp of the event occurring is offset at ∼5 mins between the guidance data and our light curve. We attribute this to calibration differences between FGS and science data.

time systematic model. In addition, we include a simple step function to account for the mirror tilt event. We explore the parameter space using the Markov Chain Monte Carlo (MCMC) sampling algorithm EMCEE (Foreman-Mackey et al. 2013) using 300 walkers, 1000 steps, and an additional 600 burn-in steps, where the starting parameter values are set as the resulting values from an initial least-squares fit.

First, we fit the NRS1 (2.87–3.72 μm) and NRS2 (3.82–5.16 μm) white-light light curves independently and retrieve the system parameters scaled stellar radius (a/R_*), inclination and mid-transit time as well as R_p/R_*. We fixed the period to 2.7347703 d (Patel & Espinoza 2022) and assumed a circular orbit ($e = 0$, $\omega = 90°$). We further fit for the step time and step amplitude to account for the mirror tilt. The retrieved system parameters and the step time for NRS1 and NRS2 were then held fixed to those values when fitting the spectroscopic light curves. These retrieved system parameters and their corresponding uncertainties are given in Table 2.

For the modelling of the limb-darkening, we use the quadratic limb-darkening law and use both limb-darkening parameters (u1, u2) as free fitting parameters in all light-curve fits, with a broad uniform prior. The fitted white light curves are shown in Fig. 2, while the spectroscopic light curves at $R = 400$ are shown in Fig. 3 together with the respective residuals.

We further conduct a combined fit of the NRS1 and NRS2 white light curves to investigate system parameters and their differences in NRS1 and NRS2. In this fit we again model the light curve using quadratic limb-darkening (freely fit for u1 and u2), a linear model and the transit model. The fitted parameters are also shown in Table 2.

3.2 ExoTiC-JEDI

ExoTiC-JEDI(Alderson et al. 2022) is an end-to-end data analysis toolkit to go from `uncal` spectroscopic files to processed planetary spectra and has been implemented in a number of exoplanet studies (e.g. Alderson et al. 2023, 2024; May & MacDonald et al. 2023; Scarsdale et al. 2024). Stages 1 and 2 act as a custom wrapper for the official JWSTpipeline (v1.13.4, context map 1364) with custom steps incorporated for bias correction, and cleaning of 1/f noise at the group level. We set the jump step level to 15σ which has been found to balance the number of detections without over-correcting for changes in flux at the group level (e.g. Alderson et al. 2023). In Stage 3, ExoTiC-JEDIperforms a series of cleaning steps. We use the data quality (DQ) flags from the JWSTpipeline that indicate 'do_not_use', 'dead', 'hot', 'saturated', 'low_qe', and 'no_gain_value' to identify bad pixels and replace them with an average of the neighbouring pixels, this results in 0.3 per cent and 0.5 per cent of pixels being replaced in NRS1 and NRS2, respectively. We then perform custom routines to remove outliers in time and spatial axis, where corrections are made using the adjacent 4 pixels either side of the effected pixel in the row (for spatial) and in the integration (for time) to the flagged pixel. For the time outliers, we use a window of ten frames and a 20σ threshold to identify outliers and for spatial variations, we use a 6σ cut-off in each integration evaluated with a 21 pixel window. We additionally correct for 1/f noise at the integration level by masking the spectral trace and subtracting the median value on a column-by-column basis. We extract the final stellar spectrum using an aperture of five times the FWHM of the PSF, which is approximately 0.7 pixels wide, resulting in a total aperture width of ∼7 pixels, and use intrapixel extraction to account for partial flux illumination on the edge pixels.

3.2.1 *Light-curve fitting*

Using ExoTiC-JEDIwe fit the light curves from NRS1 and NRS2 separately throughout the process. We first fit for our broad-band integrated light curves which span 2.87–3.72 μm for NRS1 and 3.82–5.12 μm for NRS2. In each broad-band light curve, we fit for the centre of transit time, transit depth, $a/R*$, and inclination (see Table 2), while keeping orbital period (2.7347703 d), eccentricity (0.0), and omega (90) fixed. In order to correct for the mirror tilt-event, we fit for the time of the flux jump and the amplitude of the change in flux, correcting with a simple step function. We additionally fit for standard systematics from the detector and telescope which has the following functional form,

$$S(t) = s_0 + (s_1 \times (\text{xpos} \times |\text{ypos}|)) + (s_2 \times t),$$

where s_0, s_1, and s_2 are variables to be fit for, xpos and ypos are the changing position of the spectrum on the detector calculated by cross-correlating the spectra to a template (note we take the absolute value of the y-position in this model), and t is the time array. This systematic model along with the mirror tilt step-function is then multiplied with a BATMAN light-curve model (Kreidberg 2015) using a least-squares minimizer to determine the best-fitting parameters. For our spectroscopic light curves we then fix the a/R_*, inclination and centre of transit time to those determined from the broad-band fits and fit for the transit depth in each bin. For each light-curve fit, we fix the four-parameter non-linear limb-darkening coefficients to those computed using ExoTiC-LD (Grant & Wakeford 2024) using the stellar parameters shown in Table 1 to interpolate the MPS1 stellar model grid (Kostogryz et al. 2023). The spectroscopic light curves at $R = 400$ and respective residuals are shown along the EUREKA! and TIBERIUS ones in Fig. 3. We compute the transmission spectrum for $R = 100$ and $R = 400$ allowing the systematic model and mirror tilt step-function to be freely fit in each bin. Across all of our spectroscopic bins we find that there is negligible correlated (red) noise and that our residuals bin down with the expected photon precision.

Downloaded from https://academic.oup.com/mnras/article/543/3/2442/8255897 by Imperial College London Library user on 04 November 2025

Table 2. System parameters for the transit of KELT-7 b from the *JWST* NIRSpec/G395H white light curves as fitted by the three independent reductions.

Pipeline	Detector	T_0 (BJD)	R_p/R_*	a/R_*	i (°)
Eureka!	NRS1	$2460364.395942 \pm 0.000016$	0.090375 ± 0.000053	5.5528 ± 0.0030	$83.833^{+0.0091}_{-0.0093}$
Eureka!	NRS2	$2460364.395921 \pm 0.000022$	0.090236 ± 0.000058	5.5596 ± 0.0033	$83.847^{+0.0093}_{-0.0099}$
ExoTiC-JEDI	NRS1	$2460364.396044 \pm 0.000016$	0.090069 ± 0.000032	5.551 ± 0.011	83.83 ± 0.03
ExoTiC-JEDI	NRS2	$2460364.396051 \pm 0.000020$	0.090283 ± 0.000039	5.565 ± 0.013	83.85 ± 0.04
Tiberius	NRS1	$2460364.395937 \pm 0.000015$	0.090487 ± 0.000030	5.5014 ± 0.0097	83.673 ± 0.031
Tiberius	NRS2	$2460364.395944 \pm 0.000020$	0.090294 ± 0.000038	$5.5471^{+0.0124}_{-0.0121}$	83.804 ± 0.040
Eureka! combined fit	NRS1 & NRS2	$2460364.395933 \pm 0.000013$		5.5538 ± 0.0030	83.8317 ± 0.0092
	NRS1		0.090389 ± 0.000051		
	NRS2		0.090242 ± 0.000059		
Patel & Espinoza (2022)				5.60 ± 0.07	83.92 ± 0.19

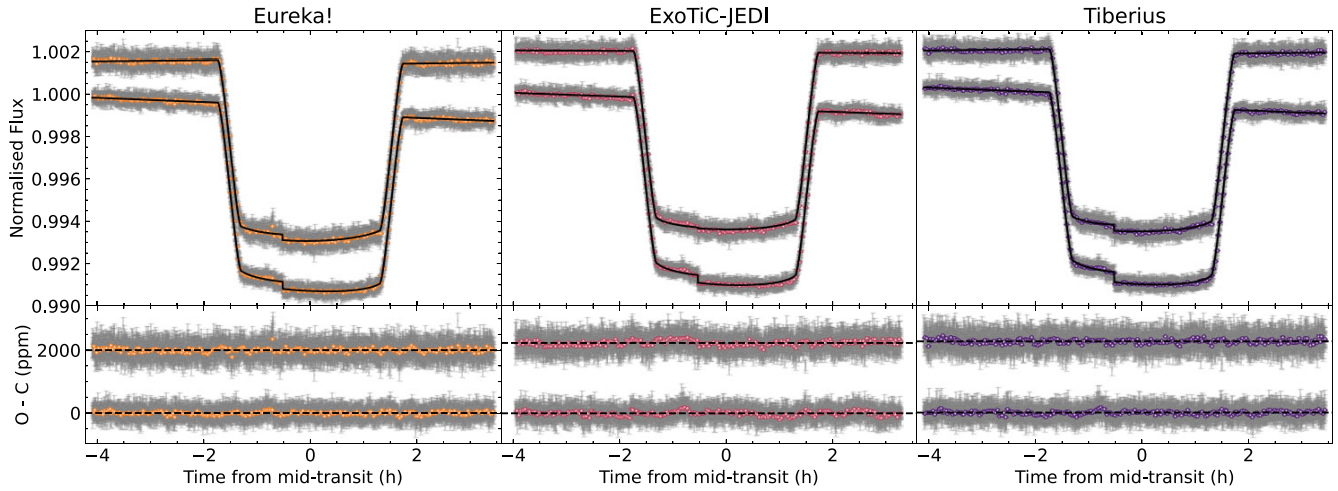


Figure 2. Top: Transit broad-band light curves of KELT-7 b with NIRSpec/G395H using Eureka!, ExoTiC-JEDI, and Tiberius (from left to right), with NRS2 being the top (offset by 0.002) and NRS1 the bottom light curve. Bottom: The corresponding residuals using the best-fitting model; the top data showing the NRS2 residuals (offset by 2000 ppm) and NRS1 residuals on the bottom.

3.3 Tiberius

We used the Tiberius (Kirk et al. 2017, 2021) *JWST* data reduction software for a third reduction, which has been used in a number of *JWST* studies (e.g. Alderson et al. 2023; Lustig-Yaeger et al. 2023; Kirk et al. 2024b). As described in Kirk et al. (2024a), we are performing one identical reduction for each BOWIE-ALIGN target to help avoid reduction-dependent biases when we combine the spectra at the end of this survey, which is this Tiberius reduction.

3.3.1 Light-curve extraction

For this reason, our Tiberius (v1.0.4) reduction used the same extraction input file, jwstpipeline version (v1.8.2), *JWST* calibration files and light-curve binning schemes as our Tiberius extractions of WASP-15b (Kirk et al. 2025) and TrES-4b (Meech et al. 2025). We refer the reader to Kirk et al. (2025) for a detailed explanation of the spectral extraction process. In brief, we perform our own 1/f correction at the group-level stage followed by custom bad pixel and cosmic ray correction routines. Finally, we perform spectral tracing using a fourth order polynomial and standard aperture photometry with an aperture full width of 8 pixels at the integration stage.

3.3.2 Light-curve fitting

For the reasons described above, we initially followed the same light-curve fitting procedure as used in previous BOWIE-ALIGN analyses. This involved fitting the white light curves with a combination of a batmananalytic transit light curve (Kreidberg 2015) from darker colour to lighter colour and a linear-in-time systematics model. However, as explained in Section 3.1.2, there is a mirror-tilt event in the transit that was not detrended by the adoption of a simple linear polynomial. For this reason, we added a step function to our systematics model, parametrized by the step position (in units of integration number) and a normalizing term which allows the systematics model to move up and down in flux after the step.

The free parameters of the transit model are the time of mid-transit (T_0), inclination of the planet (i), the ratio of semimajor axis to stellar radius (a/R_*) and ratio of planet-to-star radii ($R_p/R_\star$). Like our Eureka! reduction, we assume quadratic limb darkening however, unlike our Eureka! reduction, we fix the coefficients to the values computed with ExoTiC-LD(Grant & Wakeford 2024) and 3D stellar models (Magic et al. 2015) using the stellar parameters in Table 1. The free parameters of the systematics model were the two coefficients of the linear polynomial and the step function's breakpoint and normalizing term. Therefore, our white light-curve fits had a total of 8 free parameters. We held the planet's eccentricity fixed to 0 and the longitude of periastron to

Downloaded from https://academic.oup.com/mnras/article/543/3/2442/8255897 by Imperial College London Library user on 04 November 2025

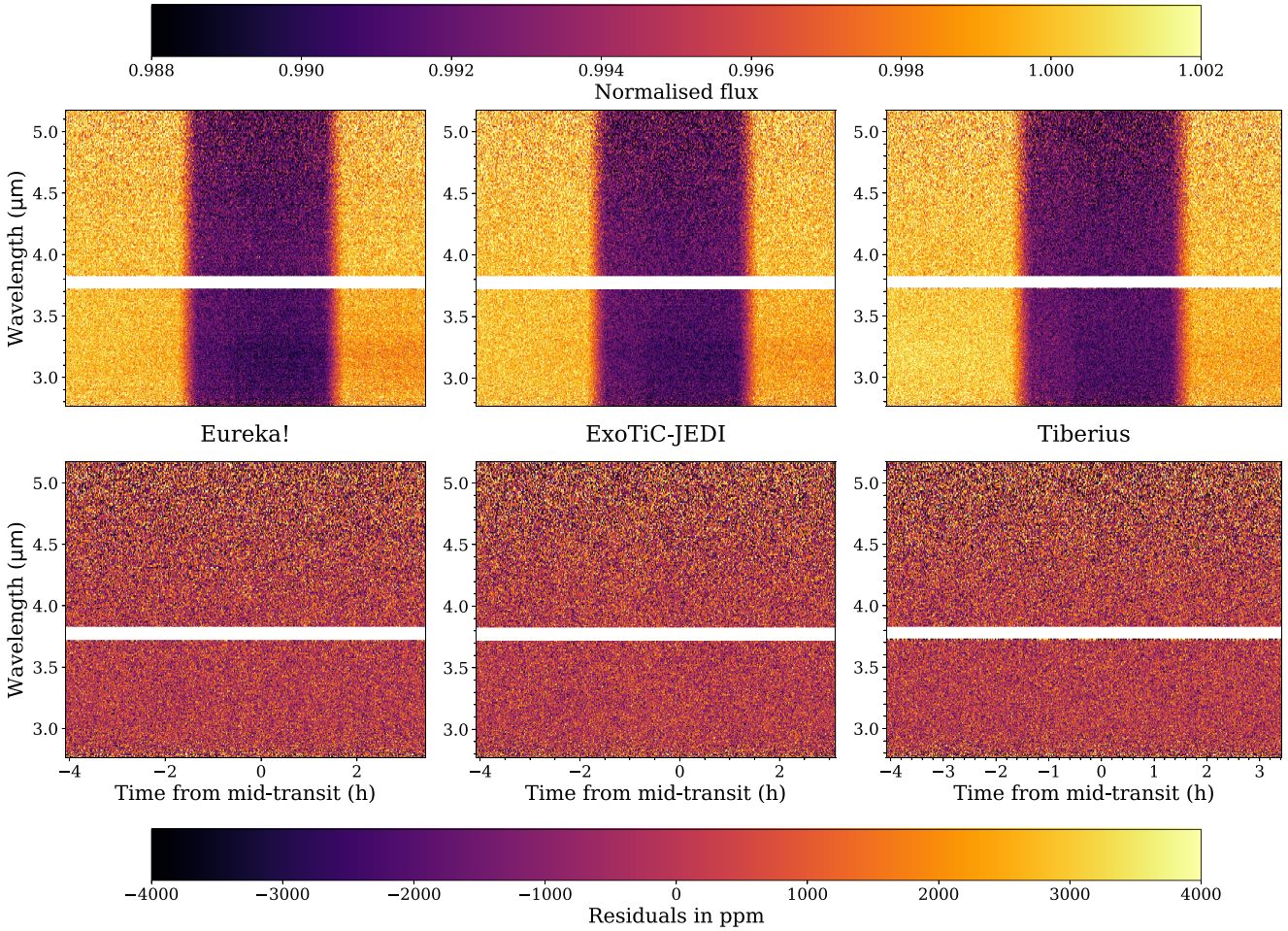


Figure 3. Extracted raw spectroscopic light curves (top row) and corresponding residuals (bottom row) of each reduction (columns; Eureka!, ExoTiC-JEDI, and Tiberius) of KELT-7 b with NIRSpec/G395H at a resolution of $R = 400$. The white area corresponds to the gap between the two detectors (NRS1 and NRS2).

90° (Bieryla et al. 2015). The period was fixed to 2.7347703 d (Patel & Espinoza 2022).

We found that Levenberg–Marquadt was unable to reliably estimate the uncertainties in the step functions' parameters. For this reason, we used MCMC sampling through emcee (Foreman-Mackey et al. 2013), unlike in our previous BOWIE-ALIGN analyses where we used Levenberg–Marquadt. We ran two sets of chains, both with 180 walkers and ran for as many steps as needed to reach $>50\tau$ where τ is the autocorrelation time. Typically, 4000 steps for each set of chains was sufficient to reach this criterion. The best fit from the first iteration was used to rescale the photometric uncertainties to give $\chi^2_\nu = 1$ for the best-fitting model. The second iteration was randomly scattered around the median values from the first iteration. We then took the medians, 16th and 84th percentiles from the final 15 000 steps of the second iteration, with a thinning factor of 10, as our parameter values and uncertainties.

The system parameters we obtain are reported in Table 2. As this Table shows, we found a disagreement between the system parameters derived from the NRS1 and NRS2 detectors, particularly $a/R_\star$ and i. This discrepancy between the two detectors' system parameters is not seen in either the Eureka! or ExoTiC-JEDIreductions. For our other BOWIE-ALIGN targets (WASP-15b and TrES-4b), we did not see this inconsistency between the detectors. In an attempt to bring these into better agreement, we experimented with 25 variations of our model, including additional systematics parameters such as x and y position, fine guide star data, free limb darkening, high order polynomials, clipping data around the step function, and choice of starting positions for the chains. None of these tests brought the NRS1/NRS2 system parameters into agreement. For this reason, we proceeded with our original model since it is as similar as possible to our other BOWIE-ALIGN analyses.

We adopted the same model and MCMC sampling procedure for our spectroscopic light-curve fits. Normally at this stage in our uniform Tiberius analyses of BOWIE-ALIGN targets, we would fix the system parameters (a/R_*, i and T_0) to the weighted mean white light values from NRS1 and NRS2. However, as discussed, these were inconsistent between NRS1 and NRS2. For this reason, we fixed the system parameters in our spectroscopic light-curve fits to the values we infer from our NRS2 white light-curve fit. We chose these values due to the better agreement with the system parameters derived from Eureka! and ExoTiC-JEDIwhich suggests the problem with the Tiberius parameters arises from NRS1, which could be related to the larger amplitude red noise for this detector and data set. At this stage, we also fixed the step function's break point, s_P, to the value from the Tiberius NRS2 white light-curve fit. This gave us four free parameters per spectroscopic light curve, $R_P/R_{*,i}$, the two coefficients of the linear polynomial and the step function

Downloaded from https://academic.oup.com/mnras/article/543/3/2442/8255897 by Imperial College London Library user on 04 November 2025

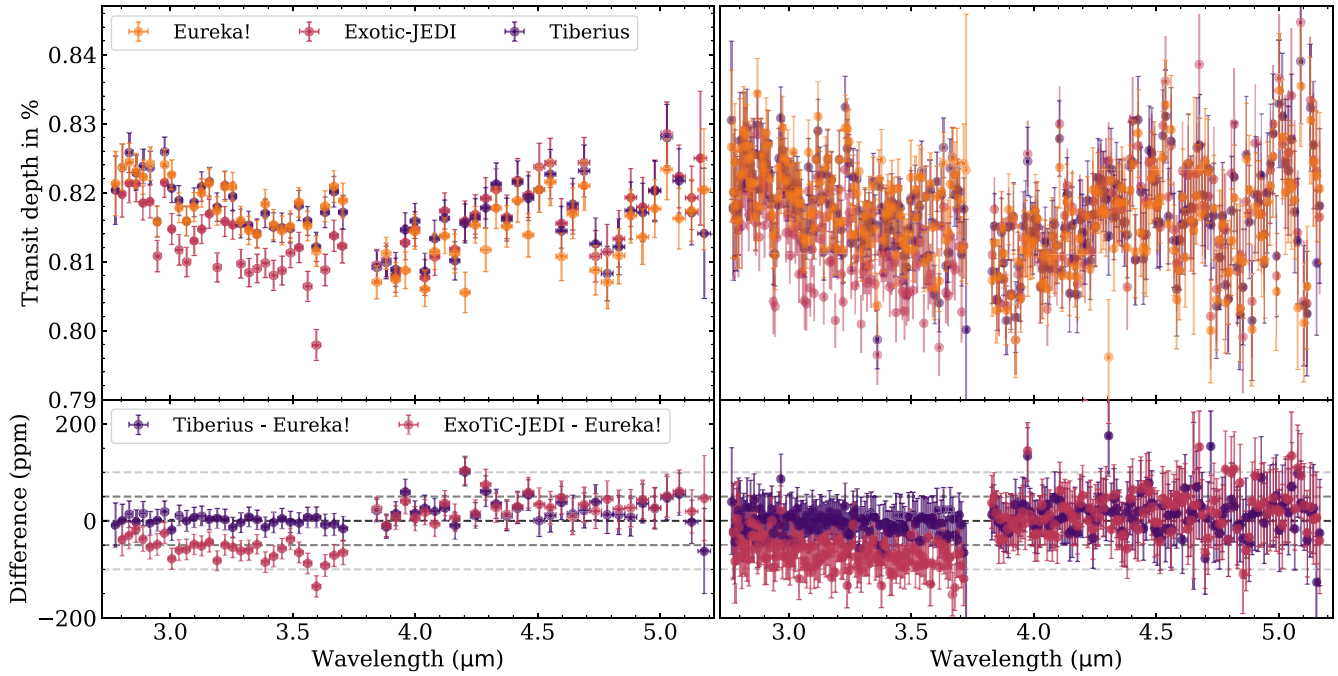


Figure 4. Top: KELT-7 b's transmission spectrum using *JWST*'s NIRSpec/G395H and three independent reductions Eureka!, Tiberius, and ExoTiC-JEDI, in two resolutions $R = 100$ (left) and $R = 400$ (right). Bottom: We find offsets between the reductions likely due to the small number of groups/integrations and mirror tilt event. The differences are shown here relative to the Eureka! reduction and horizontal lines are indicated at 0, ±50, ±100 ppm, which are typical ranges of offsets found by retrievals.

normalizing term. The light curves for the wavelength binning of $R = 400$ and the residuals following the transit model fitting are shown in the right panel of Fig. 3.

3.4 Data reduction comparisons

Fig. 4 shows the transmission spectra of KELT-7 b as determined by the three independent pipelines at resolutions $R = 100$ and $R = 400$. Note that we find offsets between the reductions and between NRS1 and NRS2, which we attribute to a combination of the low number of groups/integrations, the mirror tilt event and differences in the treatment of limb-darkening. On the other hand, when looking at the fitted NRS1 and NRS2 white light curves in Fig. 2 we find that the fitted amplitude of the step caused by the tilt event in ExoTiC-JEDI's NRS2 is much smaller compared to Eureka!'s and Tiberius'. Considering the differences between ExoTiC-JEDI and the other reductions is smaller in NRS2 than NRS1, we can likely rule out light-curve fitting as the cause for the offset.

In terms of quantitative comparisons, all three reductions showed similar transit depth precisions and scatter. The median transit depth uncertainties are 53, 50, and 51 ppm and the averages of the root mean square of the residuals are 1601, 1578, and 1613 ppm for Eureka!, ExoTiC-JEDI, and Tiberius, respectively, calculated across both NRS1 and NRS2.

The fitted system parameters did not indicate any reason for offsets between the reductions. We further tested this by retrieving a transmission spectrum using the system parameters from the combined NRS1&NRS2 white light fit using Eureka!, but this did not amount to significant offset differences, see Appendix A.

Thus, we choose to use all transmission spectra of all reductions and resolutions to investigate inferences of KELT-7 b's atmosphere, but we set our fiducial spectrum as Eureka! $R = 400$.

4 ATMOSPHERIC RETRIEVAL ANALYSIS

4.1 Retrieval set-up

We use three different atmospheric retrieval codes to interpret our *JWST* NIRSpec/G395H transmission spectrum of KELT-7 b. We use petitRADTRANS (pRT) and Poseidon to run equilibrium chemistry retrievals and free chemistry for retrievals on the *JWST* data, on all reductions and resolutions, while we use the third framework, NemesisPy, to model the panchromatic *JWST* + *HST* spectrum of KELT-7 b. For all retrieval set-ups, we fix stellar parameters to the values presented in Table 1 and planetary parameters from Table 2.

Our free chemistry set-up is further split into two cases: (1) only including near-infrared, *base* species which are H_2O, CO, CO_2, H_2S, HCN for Poseidon and two additional species (CH_4 and NH_3) for pRT, and (2) including *high temperature* species that can occur at temperatures >2000 K (SiO, VO, TiO, AlO, SH); all species are listed in Table B1 along with the references to the specific line list.

Although previous literature does not find conclusive evidence of these high-temperature species, we run an additional retrieval including them as the temperatures in the planetary atmosphere could allow for their formation. This further allows us to investigate if any features in the spectrum could be explained by these molecules, e.g. the increase in the transit depth at ∼5 μm (see Fig. 4). Note that we are excluding FeH due to the absence of opacity at infrared wavelengths.

For all retrievals, we use a grey cloud deck at pressure level $P_{\rm cloud}$, we fit for planet gravity ($\log_{10} g$) using a Gaussian prior based on the planet's radius and mass measurements, temperature (T), and an offset between NRS1 and NRS2 ($\delta_{\rm rel}$). The priors of all parameters used for each of our retrieval models are given in Table B1 for both Poseidon and pRT. We describe retrieval-specific set-ups in the following sections.

Downloaded from https://academic.oup.com/mnras/article/543/3/2442/8255897 by Imperial College London Library user on 04 November 2025

We further investigated non-isothermal P–T profiles using POSEIDON in free chemistry with IR species using the EUREKA! $R = 400$ data set. Specifically, we tested the Guillot profile (Guillot 2010) and five-parameter profile (Madhusudhan & Seager 2009), but they were disfavoured by the Bayesian evidence and the structure was indistinguishable from an isothermal profile. Therefore we used an isothermal profile for all our retrievals presented here.

In addition to our presented *JWST* results, we also conduct a retrieval analysis when combining NIRSpec with previously published *HST* data (Pluriel et al. 2020; Gascón et al. 2025) to test our conclusions. For this we use POSEIDON and NEMESISPY for free chemistry retrievals; we also conduct equilibrium retrievals using NEMESISPY, where the abundance of H^- and e^- is a free fitting parameter, as KELT-7 b's *HST* WFC3/G141 spectrum cannot be adequately fitted with H^- at equilibrium abundances only (Gascón et al. 2025). We require additional parameters in the *JWST* + *HST* retrievals to describe the optical absorption in the atmosphere. Both POSEIDON and NEMESISPY use a scattering slope parametrized by $\log a$ and γ (where a is the enhancement over Rayleigh scattering and γ tunes the strength of the scattering slope), and H^- absorption. The specific retrieval set-up by POSEIDON and NEMESISPY used for our tests using a combined *JWST* + *HST* retrievals are described in the relevant subsection for each code.

4.1.1 Poseidon-*specific set-up*

To examine the atmosphere of KELT-7 b, we implement free chemistry retrievals with the open-source package, POSEIDON (MacDonald & Madhusudhan 2017; MacDonald 2023). The model parameter space is explored with 1000 live points, using the nested sampling package PYMULTINEST (Feroz, Hobson & Bridges 2009; Buchner et al. 2014).

The atmosphere is modelled as hydrogen–helium dominated with a ratio He/H = 0.17 within which trace gaseous abundances are represented by their $\log_{10} X$ VMRs. We model our atmosphere at 100 pressure levels distributed uniformly in log space, with a maximum pressure of 100 bar. The reference pressure is fixed at 10 bar. Due to the presence of H^- in the atmosphere (inferred by the analysis of Pluriel et al. 2020; Gascón et al. 2025), we set a generous lower limit on the pressure of 10^{-10} bar in the free chemistry retrieval to capture the full contribution of any H^- opacity. The model transmission spectrum for each atmospheric model is computed at $R = 30\,000$ from 1–5.2 μm.

For the *JWST* + *HST* retrievals, POSEIDON further uses a linear wavelength grid of 10 000 points between 0.19–1 μm such that the spectral resolution across this wavelength range is >100× the resolution of the G280 data. These spectra are then convolved and binned to the resolution and wavelength solution, respectively, of our data.

4.1.2 petitRADTRANS-*specific set-up*

We used petitRADTRANS (PRT) version 3.1 (Mollière et al. 2019; Blain et al. 2024; Nasedkin, Mollière & Blain 2024) to run equilibrium chemistry retrievals, which uses a pre-calculated chemistry table from easyCHEM (Lei et al. 2025), first described in Mollière et al. (2017). Within PRT we conduct parameter exploration using the PYTHON version of the nested sampling algorithm MULTINEST (Feroz et al. 2009; Buchner et al. 2014) where we use 500 live points for exploring the space of the seven total free parameters. We use 100 atmospheric layers equally distributed in log space, from 10^{-8} to 10^2 bar. The reference pressure is fixed at 0.1 bar.

We use PRT's correlated-*k* opacity tables at $R = 1000$, for both the base species and high-temperature species. The prior ranges (in mass fractions) and references can be found in Table B1. We consider H_2–H_2 and H_2–He collision-induced absorption (Richard et al. 2012).

4.1.3 NemesisPy-*specific set-up*

NEMESISPY is a PYTHON-based version of NEMESIS, a retrieval package that uses a correlated-k (Lacis & Oinas 1991) radiative transfer model combined with PYMULTINEST (Feroz & Hobson 2008; Feroz et al. 2009; Feroz & Hobson 2013; Buchner et al. 2014) for the nested sampling retrieval. NEMESISPY (Irwin et al. 2008; Yang, Alday & Irwin 2024) is coupled with FASTCHEM to solve for equilibrium chemistry.

NEMESISPY has been used to analyse spectra of multiple transiting exoplanets, including KELT-7b as observed with *HST* (Gascón et al. 2025). Here, we perform chemical equilibrium retrievals for *HST* + *JWST* (G280+G141, NIRSpec/G395H) with H^- and e^- abundances as additional free parameters. It is therefore perfectly equipped to use for *JWST* + *HST* combined retrievals.

We use the three-parameter cloud and haze model used by MacDonald & Madhusudhan (2017) with an additional cloud fraction parameter. We retrieve the reference radius and pressure level of the reference radius, and offsets between instruments/detectors. For the full retrieval including the Hubble data sets, we use the six-parameter T-p profile from Madhusudhan & Seager (2009); we also include offsets for G141, NRS1, and NRS2 relative to G280, and the same stellar activity parametrization we use in Gascon et al. (under review), retrieving the photospheric temperature, the temperature of any heterogeneities, and the heterogeneity filling factor. For the NIRSpec-only retrieval, we adopt an isothermal T-p profile and retrieve the offset for NRS2 relative to NRS1, and we do not include any parametrization for stellar heterogeneities. Note that for this investigation we used the EUREKA! $R = 400$ spectrum.

5 RESULTS

We discuss our results on our NIRSpec/G395H EUREKA! R = 400 transmission spectrum, which acts as the primary reduction in our retrieval analysis. To test the robustness of our free chemistry retrieval results to the choice of reduction, we also retrieve the base species and high-temperature species model on all other reductions and resolutions. While we do not discuss these separately, we note any differences in retrieval outputs when applied to different reductions or resolutions.

5.1 Equilibrium chemistry

KELT-7 b's atmosphere retrieved using pRT and POSEIDON chemical equilibrium set-ups shows wide ranges for the atmospheric C/O and metallicity. The best fit and the opacity contributions are shown in Fig. 5. The C/O ratios retrieved for all reductions and resolutions demonstrate a range from 0.43–0.74, with relatively large uncertainties of up to 0.32 and do not exhibit a Gaussian shape, see Fig. 6 and Table 3. They all agree well within the 1σ for that reason and no direct constraints can be placed on the atmospheric C/O ratio of KELT-7 b. Though, we note that all posteriors from the reductions consistently drop off sharply at a C/O ratio greater than 0.9–1 at the $\sim 2\sigma$ level.

Downloaded from https://academic.oup.com/mnras/article/543/3/2442/8255897 by Imperial College London Library user on 04 November 2025

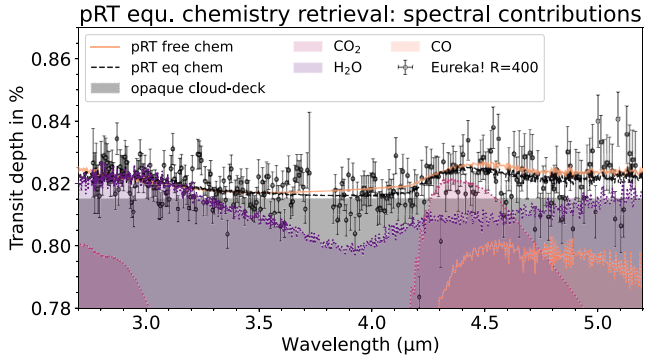


Figure 5. NIRSpec/G395H transmission spectrum of KELT-7 b using EUREKA! $R = 400$ (data points) compared to the best-fitting equilibrium (orange-dashed line) and free chemistry (magenta solid line) model using PRT. The molecular contributions (from darker colour to lighter colour: H_2O, CO_2 and CO) to the retrieved spectrum from the best-fitting equilibrium chemistry model are shown, as well as the grey cloud-deck (grey-shaded box).

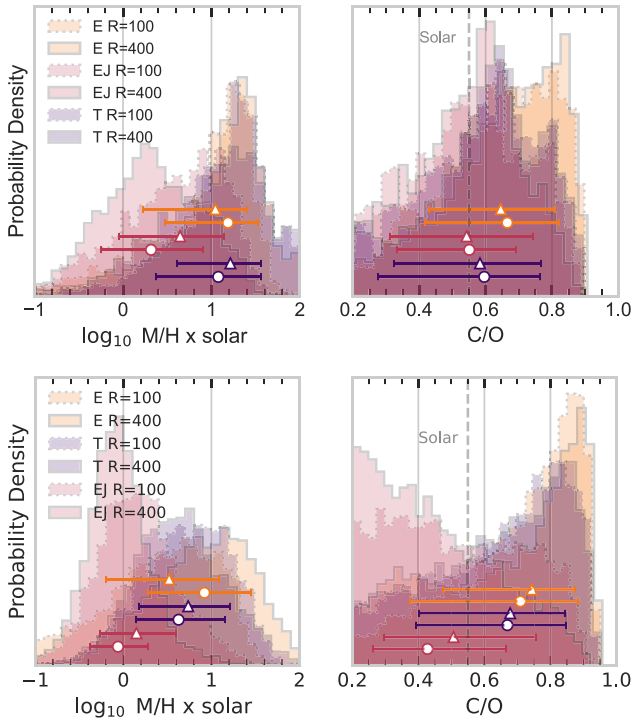


Figure 6. Retrieved C/O and metallicity for KELT-7 b from the PRT equilibrium chemistry retrievals (top) and POSEIDON (bottom), showing each of the reductions [EUREKA! (E), EXOTIC-JEDI (EJ), TIBERIUS (T)] at both $R = 100$ and $R = 400$ spectral resolutions. The markers ($R = 100$: triangle; $R = 400$: round) correspond to the median value, the errors to the 16th and 84th percentile.

The metallicities retrieved in the equilibrium chemistry run for both PRT and POSEIDON also display large uncertainties and their median values range from approximately solar to $\sim 15\times$ solar. The retrieval codes vary slightly in their metallicities, PRT preferring higher metallicities than POSEIDON, however, similar to the C/O ratio this is all within the 1–2σ uncertainties as the spectrum does not allow for tighter constraints. In Fig. 8, we show the computed corresponding range of VMRs for each molecule based on the retrieved C/O ratios and metallicities for KELT-7 b's atmosphere.

Table 3. Retrieved C/O ratios and metallicities of KELT-7 b's atmosphere in chemical equilibrium. Solar refers to Asplund et al. (2009).

Reduction	C/O	Z (×solar)
Equilibrium chemistry: PRT		
EUREKA! $R = 100$	$0.65^{+0.17}_{-0.22}$	$11.1^{+14}_{-9.4}$
EUREKA! $R = 400$	$0.67^{+0.16}_{-0.25}$	15^{+18}_{-13}
TIBERIUS $R = 100$	$0.58^{+0.19}_{-0.26}$	16^{+20}_{-13}
TIBERIUS $R = 400$	$0.59^{+0.17}_{-0.32}$	$11.9^{+25}_{-9.6}$
EXOTIC-JEDI $R = 100$	$0.54^{+0.20}_{-0.24}$	$4.4^{+9.6}_{-3.6}$
EXOTIC-JEDI $R = 400$	$0.55^{+0.15}_{-0.22}$	$2.1^{+6.0}_{-1.6}$
Equilibrium chemistry: POSEIDON		
Reduction	C/O	Z (×solar)
EUREKA! $R = 100$	$0.74^{+0.13}_{-0.27}$	$3.2^{+17.0}_{-0.9}$
EUREKA! $R = 400$	$0.71^{+0.17}_{-0.33}$	$8.3^{+37.2}_{-2.5}$
TIBERIUS $R = 100$	$0.68^{+0.17}_{-0.28}$	$5.5^{+20.0}_{-1.8}$
TIBERIUS $R = 400$	$0.67^{+0.18}_{-0.28}$	$4.2^{+12.6}_{-1.2}$
EXOTIC-JEDI $R = 100$	$0.51^{+0.25}_{-0.21}$	$1.4^{+3.5}_{-0.5}$
EXOTIC-JEDI $R = 400$	$0.43^{+0.24}_{-0.16}$	$0.9^{+1.8}_{-0.4}$

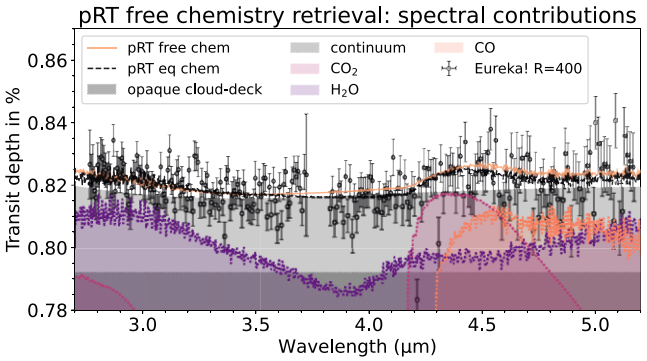


Figure 7. Similar to Fig. 5, NIRSpec/G395H transmission spectrum of KELT-7 b using EUREKA! $R = 400$ (data points) compared to the best-fitting equilibrium (dashed line) and free chemistry (solid line) model using PRT. Here, the molecular contributions (median) are shown from the free chemistry retrieval, from dark to light colouring: H_2O (dotted), CO_2 (dotted), CO (dotted). The free chemistry retrievals (both POSEIDON and PRT) find a low altitude cloud deck and low abundance of infrared species, probing the continuum opacity level, thus, we also include the continuum's contribution (off the plot axis in the equilibrium chemistry case). The grey cloud-deck is indicated by the lighter-shaded box, the continuum is the darker-shaded box.

We find the best fit to be an atmosphere with a high-altitude cloud-deck, consistent across reductions, with a tail towards lower altitudes. The wide, unconstrained nature of the cloud-deck for both POSEIDON and PRT likely contributes to the large uncertainties in C/O and metallicity as any abundances are challenging to constrain if the amount of cloud opacity is unknown. This is demonstrated by the fact, that this high-altitude cloud layer by the equilibrium chemistry retrievals is contrary to our results from free chemistry models with low-altitude clouds (see Section 5.2). The temperature also shows a large range of possible solutions with the 1σ contours spanning a range of ~1000 K. Cloud deck layer and temperature show a slight correlation in our posteriors, where the higher cloud deck altitudes are associated with higher temperatures (>1300 K), more consistent with KELT-7 b's equilibrium temperature. The posterior plots for

Downloaded from https://academic.oup.com/mnras/article/543/3/2442/8255897 by Imperial College London Library user on 04 November 2025

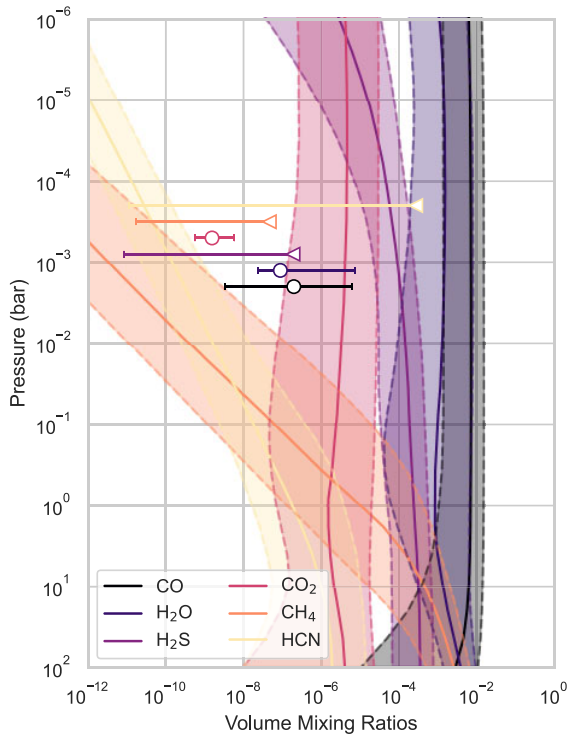


Figure 8. Pressure and VMRs; a comparison between the retrieved values through free chemistry (points with 1σ uncertainties for CO, H_2O, and CO_2 and 2σ range as an upper limit for the remaining unconstrained species) and the profiles calculated based on the retrieved C/O ratio and metallicity from the equilibrium chemistry model (using their 1σ uncertainties), both with pRT. The individual colours correspond to the molecules included in the model.

both retrievals and all three reductions at $R = 400$ are displayed in the Appendix, Figs D3 and D4 for Poseidon and pRT, respectively.

5.2 Free chemistry

5.2.1 *Base model*

The free chemistry base model (only including near-infrared species, see Section 4) retrieves low abundances for H_2O and CO_2 using both Poseidon and pRT. Best-fitting temperatures for Poseidon and pRT vary: while the former retrieves a temperature of ∼1600 K, pRT favours a temperature ∼2000 K, though both are poorly constrained with uncertainties of >500 K. In Poseidon, we also find a bimodal temperature distribution, where a very low temperature (<900 K, pushing the lower prior bound), high mean molecular weight solution, with high abundance modes of CO and CO_2 (pushing the upper prior boundaries) also able to provide a good fit to the data. These high atmospheric CO and CO_2 fractions of the order of 0.1 cannot be explained physically for a hot Jupiter of this density, nor does the temperature mode correspond to a realistic limb average temperature for a $T_{eq} = 2048$ K planet. This mode is not correlated with the remaining species in the model. VMRs of H_2O, CO_2, and CO and detection significances using Bayesian evidence differences for both retrievals are listed in Table 4.

Poseidon retrieves an atmosphere that is cloud-free, with a lower cloud deck pressure level at $\log_{10} P_{cloud} = 0.63^{+0.90}_{-0.94}$ bar. pRT also retrieves this solution for the cloud-deck (at $\log_{10} P_{cloud} \sim 0.38$), but an additional mode is also seen at $\log_{10} P_{cloud} \sim -3.5$ which is consistent with the preferred cloud-top pressure by the equilibrium chemistry models. The combination of a low altitude cloud deck and low abundance of infrared species means that the spectrum is probing the continuum opacity level, clearly visible in Fig. 7 which displays the molecular as well as continuum contributions to the transmission spectrum.

Table 4. Retrieved volume mixing ratios (VMRs) for H_2O, CO_2, and CO from our Poseidon and pRT retrievals, where the uncertainties refer to the 1σ confidence intervals. The detection significances for each detected species are shown here as the differences in Bayesian evidence values $\Delta \ln \mathcal{Z}$, where $1.0 < \Delta \ln \mathcal{Z} < 2.5$ is considered weak to tentative evidence for a detection and $\Delta \ln \mathcal{Z} < 1.0$ is considered inconclusive (Jeffreys 1983). The model including CO for Poseidon is not preferred at all as $\Delta \ln \mathcal{Z} < 0$.

Eureka! $R = 400$	H_2O	CO_2	CO
Poseidon			
$\log_{10}$(VMR)	$-7.05^{+0.67}_{-1.96}$	$-8.46^{+6.02}_{-0.28}$	$-7.23^{+4.85}_{-2.76}$
$\Delta \ln \mathcal{Z}$	1.9	1.5	−0.7
pRT			
$\log_{10}$(VMR)	$-7.05^{+0.59}_{-1.93}$	$-8.81^{+0.44}_{-0.58}$	$-6.7^{+1.8}_{-1.6}$
$\Delta \ln \mathcal{Z}$	1.0	0.9	0.3

Each reduction finds broadly consistent parameters to the Eureka! $R = 400$ reduction – all atmospheric parameters fall within 1σ of each other. The high mean molecular weight, low temperature mode is only visible using Poseidon and is most prominent for the Eureka! $R = 400$ reduction, though still present to a lesser extent in the remaining reductions. The high altitude cloud-top pressure mode is mostly also recovered in the other reductions when using pRT; only ExoTiC-JEDI $R = 400$ does not show a peak in the posterior distribution in that parameter space. The posterior distributions of this base model using free chemistry for both Poseidon and pRT with the different reduction can be found in the Appendix, Figs D1 and D2, respectively.

5.2.2 *Model with high-temperature species*

The spectrum retrieved by Poseidon when including the high-temperature species and the retrieved parameters are displayed together with the retrieval with only the base species in Fig. 9. For both Poseidon and pRT, the atmosphere that is retrieved produces a slightly smaller offset (15–20 ppm smaller) between NRS1 and NRS2. It is characterised by high abundances of all molecules, specifically H_2S, CO, and VO, with H_2O and SH pushing toward the upper prior bound. The spectral decomposition (bottom left, Fig. 9) shows that the flattening of the H_2O slope is being produced by the high H_2S abundance, exhibiting the same shape as a low H_2O abundance and continuum opacity. At the edge of the NRS2 detector, around 5 μm, the transit depths increase which is fit by opacity from the high VO ($\log_{10}$ VMR $= -2.79^{+0.77}_{-3.23}$), which is physically unrealistic.

pRT shows a statistical preference for the base species model as the Bayesian evidence for the model including the high-temperature species decreases by $\Delta \ln \mathcal{Z} = 2.0$. In contrast, Poseidon statistically prefers the high temperature species model with $\Delta \ln \mathcal{Z} = 2.44$. However, it is unlikely that such species could exist at the high abundances inferred by the retrieval and they are not detected at optical wavelengths in Gascón et al. (2025) where their opacity should be most prominent. Therefore, with pRT finding no evidence for high-T species and Poseidon producing a physically implausible atmosphere, we conclude it is unlikely that any molecules that form

Downloaded from https://academic.oup.com/mnras/article/543/3/2442/8255897 by Imperial College London Library user on 04 November 2025

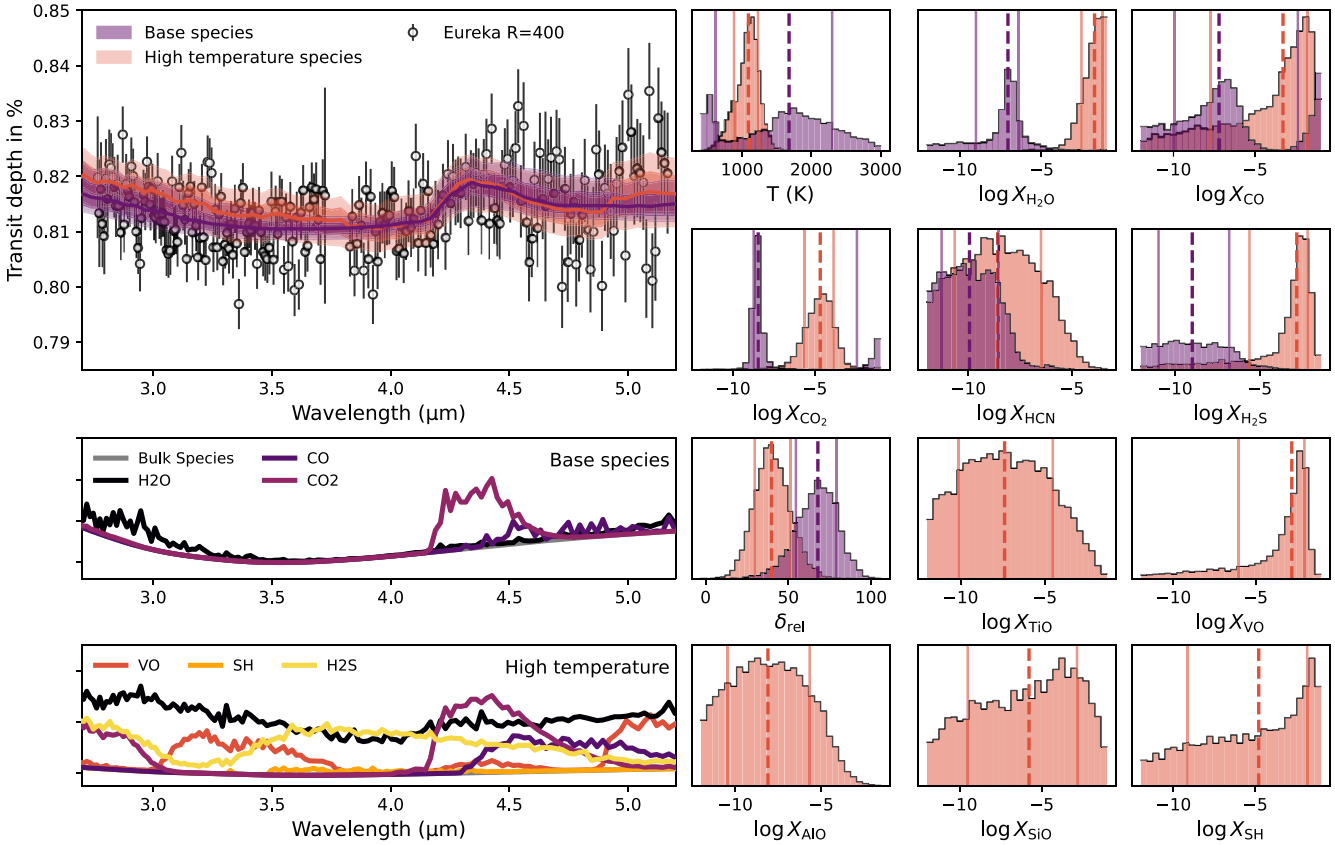


Figure 9. Comparison between the free chemistry retrievals using the *base* species as well as including *high-temperature* species. Top left panel: *JWST* NIRSpec/G395H transmission spectrum of KELT-7b using Eureka! $R = 400$ and the two competing free chemistry retrievals (base species and high-temperature species). Bottom left panels: Spectral contributions of the fitted species for the two models considered. Right panels: posterior distributions of the fitted retrieval parameters. While the high temperature species are statistically favoured it produces unrealistically high abundances for a number of species and thus we rule it out for KELT-7b.

at the high temperature regime are contributing to the opacity in KELT-7 b's NIRSpec transmission spectrum.

5.2.3 *Combined with HST*

To be able to distinguish between the two preferred models, we investigate whether the previously published two *HST* data sets in the UV and IR can aid in constraining the continuum and/or cloud layer, as well as the H_2O abundance. However, as the wavelength ranges of none of the data sets overlap, the offset between the spectra is unknown. In addition, the H^- in the atmosphere of KELT-7 b and the lack of knowledge of abundance constraints on said H^- prohibit any inference about the continuum or cloud level.

Therefore, our free chemistry retrievals with *JWST* + *HST* combined is not able to provide further constraints on the atmospheric composition of KELT-7 b. We find good agreement in the retrieved atmospheric parameters in the free chemistry model, see Fig. 10. Similarly, the metallicity and C/O ratio in the equilibrium chemistry model with free H^- and e^- is consistent and shows equally wide posteriors compared to the NIRSpec-only retrieval, see Appendix, Fig. E1.

6 DISCUSSION AND CONCLUSIONS

We present the transmission spectrum of the aligned hot Jupiter KELT-7 b obtained from a single transit observation with *JWST* NIRSpec/G395H, covering the 2.8–5.2 μm wavelength ranges. We find evidence for a mirror-tilt event in our data, also visible in the *JWST* fine guidance data. The time-series spectra were reduced using three independent pipelines, which showed offsets between each other, likely a combination of the uncertainty in flux change due to the mirror-tilt event and the low number of groups/integration (5) causing higher noise.

We find that our transmission of KELT-7 b shows only weak features of H_2O and CO_2. To draw inferences about KELT-7 b's atmosphere based on our NIRSpec/G395H spectrum, we use two independent atmospheric retrieval codes, pRT and Poseidon, and apply equilibrium and free chemistry set-ups. With our retrieval set-ups, we find two competing scenarios for the atmosphere of KELT-7 b: (1) a cloud layer at high altitude and small features, or (2) a cloud-free low-metallicity atmosphere where we probe the continuum layer. Since the simpler, equilibrium chemistry model is statistically preferred (see $\ln \mathcal{Z}$ in Table C1) in all reductions, resolutions and retrieval set-ups at $\Delta \ln \mathcal{Z} = 1.6$–$3.1$, the slightly preferred scenario is that KELT-7 b's atmosphere has a (1) relatively high cloud-deck which masks the molecular features. Based on KELT-7 b's equilibrium temperature of 2050 K, cloud condensate species such as SiO_2 or Al_2O_3 can form and explain the high-altitude cloud deck (e.g. see Wakeford & Sing 2015; Parmentier et al. 2016). We further tested cloud fraction as a free parameter to allow for patchy clouds, though it was not statistically preferred (Bayesian evidence difference at $\Delta \ln(\mathcal{Z}) \sim 1$). We note the inclusion of these

Downloaded from https://academic.oup.com/mnras/article/543/3/2442/8255897 by Imperial College London Library user on 04 November 2025

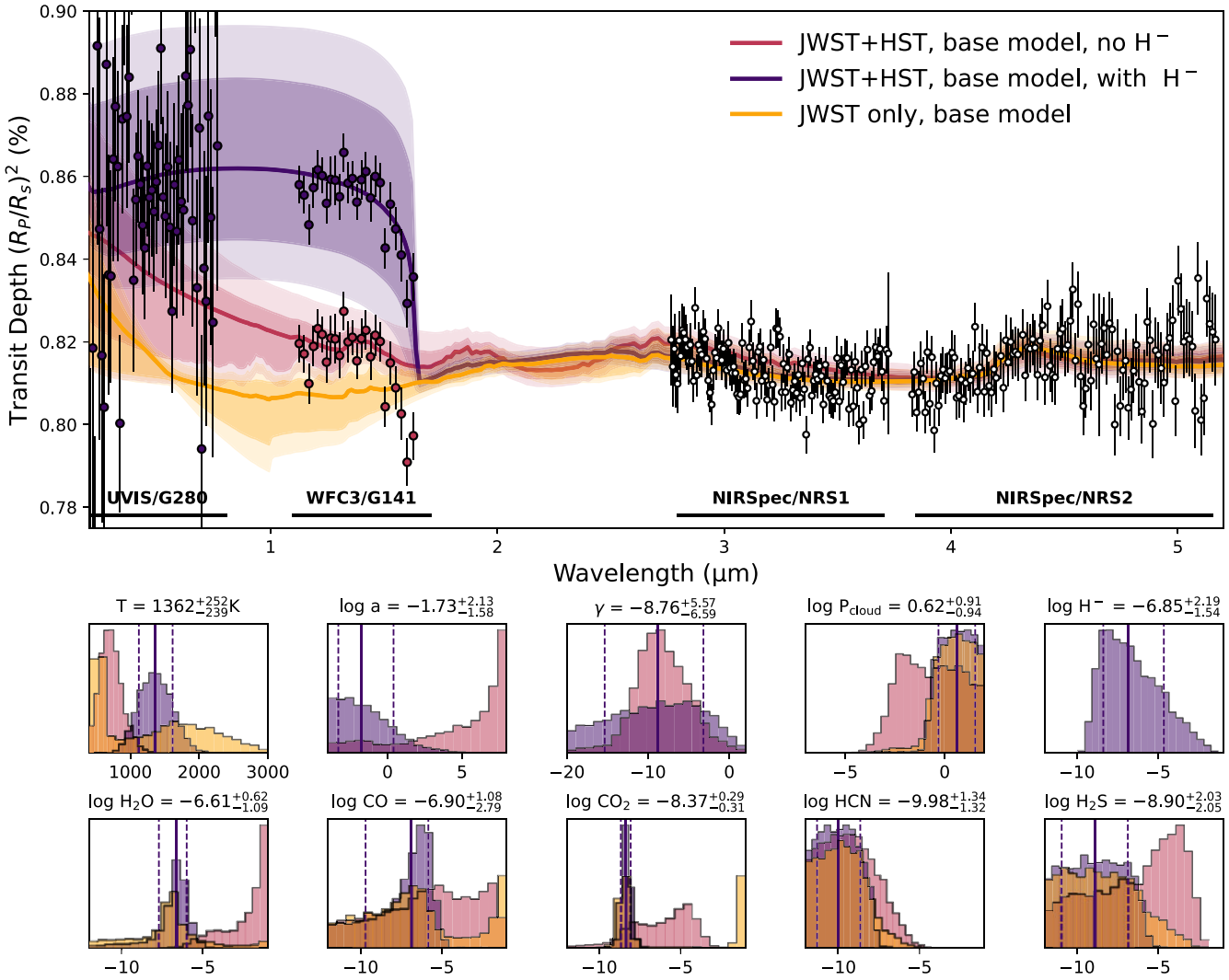


Figure 10. Top: POSEIDON free chemistry retrievals comparison between using only *JWST* data (orange) and in combination with previously published *HST* data (pink: excluding H^-; purple: including H^-). For clarity, we include the WFC/G141 data twice, as the difference in offset retrieved when including H^- is significant. The colour of the data corresponds to the offset applied from each model. For the UVIS/G280 data we only applied one offset as the uncertainties are relatively large and the offset difference is not as significant. Bottom: The posterior plots for the retrieved species, cloud deck and temperature (T), as well as scattering slope parameters for the retrievals with *HST* data ($\log a$, γ). The colours correspond to the individual models, demonstrating that the inclusion of *HST* data does not provide further constraints for the cloud deck or abundances as the unknown H^- abundance in combination with the lack of overlapping wavelengths prevents inferences about the continuum of KELT-7 b's atmosphere. Quoted median values and 1σ errors correspond to the posteriors retrieved on the *JWST* and *HST* data when including H^- opacity, shown with the vertical solid and dashed lines.

patchy clouds resulted in a preference for a cloud deck at higher altitude and a higher metallicity atmosphere.

We investigate evidence for H_2O, CO_2, and CO in our transmission spectrum of KELT-7 b. However, we are not able to detect strong evidence for any of the molecules using our free chemistry set-up. We attribute this to the small feature sizes, the unknown cloud layer and the unknown NRS1/NRS2 offset that we need to fit for. We also find a potential feature in our transmission spectrum at ∼5 μm that could be of atmospheric origin. We investigated species that may form at the higher temperatures possible on the dayside of KELT-7 b and our free chemistry retrieval suggests VO as a possible absorber. However, the retrieved abundance is relatively high. In addition, VO has not been detected in KELT-7 b's optical transmission spectrum (Gascón et al. 2025) and therefore unexpected to be detected in KELT-7 b's NIRSpec/G395H spectrum.

We extend our free chemistry retrieval analysis to *HST* wavelength ranges, as *HST* UVIS/G280 (Gascón et al. 2025) and WFC3/G141 (Pluriel et al. 2020) transmission spectra are available for KELT-7 b. However, even the addition of these data did not result in a clear indication of the cloud layer due to the unknown H- opacity and the fact that we are unable to constrain the offset between the transmission spectra from the different detectors (see Fig. 10). We find similar conclusions when running equilibrium chemistry retrievals with free H-/e-; the posteriors between the *JWST* only and *JWST* + *HST* combined retrieval are nearly identical (see Fig. E1).

Due to the lack of strong features, we are unable to place meaningful constraints on the C/O ratio of KELT-7 b's atmosphere, though all reductions show sharp drop at C/O ratios >0.9–1 at a ∼2σ level. Due to the evidence for H^- in the *HST* wavelength range, it is likely that any modelling to measure C/O needs to take the amount of

Downloaded from https://academic.oup.com/mnras/article/543/3/2442/8255897 by Imperial College London Library user on 04 November 2025

water dissociation in the upper atmosphere into account. Therefore, we are unable to quote a C/O ratio for the atmosphere of KELT-7 b. As a result, this does not place strong constraints on KELT-7 b's history as the C/O ratio we retrieve of 0.25–0.9 is consistent with many possible formation scenarios.

The retrieved metallicity of KELT-7 b's atmosphere compared to solar, $[Z/H] = -0.2$–1.5 dex, is likely stellar or super-stellar: the star KELT-7 has a metallicity of [Fe/H] $= 0.139^{+0.075}_{-0.081}$ dex (Bieryla et al. 2015). A super-stellar planetary metallicity can be created by various processes. These include an enhancement of any solid accretion through pebbles or planetesimals (e.g. Danti, Bitsch & Mah 2023; Penzlin et al. 2024); or the planet accreting significant fraction of its gaseous envelope at a location and time where the gas-phase metallicity is enhanced, e.g. near an ice line where volatiles are preferentially released from drifting pebbles (Booth et al. 2017; Bitsch & Mah 2023) or in a region where the metallicity is enhanced by disc photoevaporation (Lienert, Bitsch & Henning 2024). While this single planet does not constrain any specific scenario, it is an important piece in the puzzle to construct a comprehensive sample of similar planets in the BOWIE-ALIGN programme. The aim the programme, to probe whether the atmospheric compositions of aligned (disc-migrated) and misaligned (high-e migrated) hot Jupiters differ significantly, may only succeed when studying a population instead of individual planets (Kirk et al. 2024a).

We caution that one-transit observations with NIRSpec/G395H may not be sufficient to constrain H_2O and CO_2 in the atmosphere of a hot Jupiter which may exhibit temperatures closer to ultra-hot Jupiters where H_2O dissociation takes an effect as demonstrated by this study. Ultra-hot Jupiters observed with *JWST* include WASP-121b (T_{eq} ~ 2300 K), where observations with NIRSpec/G395H also find weak evidence for H_2O and no evidence for CO_2 in the atmosphere, though strong SiO and CO features (Gapp et al. 2025). Lothringer et al. (2025) find a NIRSpec/G395H spectrum similar to WASP-121b for ultra-hot Jupiter WASP-178b (T_{eq} ~ 2500 K; weak H_2O, no CO_2, detection of CO and SiO). In contrast to KELT-7 b, Lothringer et al. (2025) find that meaningful abundance constraints were possible when the *JWST* data was combined with the short-wavelength *HST* observations as WASP-178b shows strong absorption in the UV (<0.3 μm).

This provides a challenge when trying to constrain C/O ratios and atmospheric metallicity of ultra-hot Jupiters solely from the near-infrared wavelength ranges. Wider wavelength observations hold the key to constraining the cloud layer and determining the chemical composition present in KELT-7 b's atmosphere. However, obtaining overlapping wavelength ranges is crucial. As is the case with our study of KELT-7 b, adding *HST* UVIS/G280 and WFC3/G141 data to NIRSpec/G395H may not be sufficient to disentangle the continuum from other atmospheric processes (in this case H^-). Both additional optical and mid-infrared wavelength ranges will be valuable in constraining the cloud-deck layer, the H^- contribution, and ultimately the abundance of carbon- and oxygen-bearing molecules.

ACKNOWLEDGEMENTS

We thank the anonymous referee for their time to review this manuscript and for their valuable comments that improved this manuscript.

This work is based on observations made with the NASA/ESA/CSA *JWST*. The data were obtained from the Mikulski Archive for Space Telescopes at the Space Telescope Science Institute, which is operated by the Association of Universities for Research in Astronomy, Inc., under NASA contract NAS 5–03127 for *JWST*. These observations are associated with programme #3838. This work was inspired by collaboration through the UK-led BOWIE + collaboration. Support for programme JWST-GO-3838 was provided by NASA through a grant from the Space Telescope Science Institute, which is operated by the Association of Universities for Research in Astronomy, Inc., under NASA contract NAS 5–03127.

We are grateful to the HUSTLE programme team (GO-17183, PI: Wakeford) for providing us the *HST* UVIS/G280 transmission spectrum of KELT-7b before publication of their manuscript.

JK acknowledges financial support from Imperial College London through an Imperial College Research Fellowship grant. HRW was funded by UK Research and Innovation (UKRI) framework under the UK government's Horizon Europe funding guarantee for an ERC Starter Grant [grant no. EP/Y006313/1]. RAB and AP thank the Royal Society for their support in the form of a University Research Fellowship. AP acknowledges funding from the European Union under the European Union's Horizon Europe Research and Innovation Programme 101124282 (EARLYBIRD). Views and opinions expressed are, however, those of the authors only and do not necessarily reflect those of the European Union or the European Research Council. Neither the European Union nor the granting authority can be held responsible for them. PJW acknowledges support from the UK Science and Technology Facilities Council (STFC) through consolidated grant ST/X001121/1. NJM, DES, and MZ acknowledge support from a UK Research and Innovation (UKRI) Future Leaders Fellowship (grant MR/T040866/1), a Science and Technology Facilities Funding Council Nucleus Award (grant ST/T000082/1), and the Leverhulme Trust through a research project grant (RPG-2020-82). JEO is supported by a Royal Society University Research Fellowship. This project has received funding from the European Research Council (ERC) under the European Union's Horizon 2020 research and innovation programme (grant agreement no. 853022). JKB is supported by a UK Science and Technology Facilities Coundil Ernest Rutherford Fellowship (ST/T004479/1).

DATA AVAILABILITY

The data are available on the Mikulski Archive for Space Telescopes at the Space Telescope Science Institute, under programme number #3838. The specific observations analysed can be accessed via https://doi.org/10.17909/a3r9-tv81. The data products and posterior plots associated with this manuscript are available on Zenodo via https://doi.org/10.5281/zenodo.17092001.

REFERENCES

Ahrer E.-M. et al., 2023, Nature, 614, 653
Ahrer E.-M. et al., 2025, MNRAS, 540, 2535
Albrecht S. et al., 2012, ApJ, 757, 18
Alderson L., Grant D., Wakeford H., 2022, Exo-TiC/ExoTiC-JEDI: v0.1-beta-release, Zenodo, Version v0.1
Alderson L. et al., 2023, Nature, 614, 664
Alderson L. et al., 2024, AJ, 167, 216
Andrae R. et al., 2023, A&A, 674, A27
Asplund M., Grevesse N., Sauval A. J., Scott P., 2009, ARA&A, 47, 481
Azzam A. A., Tennyson J., Yurchenko S. N., Naumenko O. V., 2016, MNRAS, 460, 4063
Barber R. J., Strange J. K., Hill C., Polyansky O. L., Mellau G. C., Yurchenko S. N., Tennyson J., 2014, MNRAS, 437, 1828
Beatty T. G. et al., 2024, ApJ, 970, L10
Bell T. J. et al., 2022, J. Open Source Softw., 7, 4503
Bell T. J. et al., 2023, Nature, 623, 709
Bieryla A. et al., 2015, AJ, 150, 12
Bitsch B., Mah J., 2023, A&A, 679, A11

Downloaded from https://academic.oup.com/mnras/article/543/3/2442/8255897 by Imperial College London Library user on 04 November 2025

Blain D., Mollière P., Nasedkin E., Blain D., Mollière P., Nasedkin E., 2024, J. Open Source Softw., 9, 7028
Booth R. A., Clarke C. J., Madhusudhan N., Ilee J. D., 2017, MNRAS, 469, 3994
Buchner J. et al., 2014, A&A, 564, A125
Cannon A. J., Pickering E. C., 1918, Ann. Harv. College Observatory, 91, 1
Cannon A. J., Pickering E. C., 1993, VizieR On-line Data Catalog: III/135A. Originally published in: Harv. Ann. 91–100 (1918-1924), 3135, III/135A
Changeat Q. et al., 2022, ApJS, 260, 3
Coles P. A., Yurchenko S. N., Tennyson J., 2019, MNRAS, 490, 4638
Danti C., Bitsch B., Mah J., 2023, A&A, 679, L7
Deal D., Espinoza N., 2024, J. Open Source Softw., 9, 6202
Dobbs-Dixon I., Cowan N. B., 2017, ApJ, 851, L26
Espinoza N., Fortney J. J., Miguel Y., Thorngren D., Murray-Clay R., 2017, ApJ, 838, L9
Feroz F., Hobson M. P., 2008, MNRAS, 384, 449
Feroz F., Hobson M. P., 2013, MNRAS, 437, 3540
Feroz F., Hobson M. P., Bridges M., 2009, MNRAS, 398, 1601
Foreman-Mackey D., Hogg D. W., Lang D., Goodman J., 2013, PASP, 125, 306
Gaia Collaboration, 2023, A&A, 674, A1
Gapp C. et al., 2025, AJ, 169, 341
Gascón C. et al., 2025, AJ, 170, 178
Gorman M. N., Yurchenko S. N., Tennyson J., 2019, MNRAS, 490, 1652
Grant D., Wakeford H. R., 2024, J. Open Source Softw., 9, 6816
Guillot T., 2010, A&A, 520, A27
Helling C. et al., 2016, MNRAS, 460, 855
Horne K., 1986, PASP, 98, 609
Irwin P. G. J. et al., 2008, J. Quant. Spec. Radiat. Transf., 109, 1136
Jeffreys H., 1983, Theory of Probability, International Series of Monographs on Physics. Clarendon Press, Oxford
John T. L., 1988, A&A, 193, 189
Kirk J., Wheatley P. J., Louden T., Doyle A. P., Skillen I., McCormac J., Irwin P. G. J., Karjalainen R., 2017, MNRAS, 468, 3907
Kirk J. et al., 2021, AJ, 162, 34
Kirk J. et al., 2024a, RAS Tech. Instrum., 3, 691
Kirk J. et al., 2024b, AJ, 167, 90
Kirk J. et al., 2025, MNRAS, 537, 3027
Kitzmann D., Heng K., 2018, MNRAS, 475, 94
Kostogryz N., Shapiro A. I., Witzke V., Grant D., Wakeford H. R., Stevenson K. B., Solanki S. K., Gizon L., 2023, Res. Notes Am. Astron. Soc., 7, 39
Kreidberg L., 2015a, PASP, 127, 1161
Lacis A. A., Oinas V., 1991, J. Geophys. Res., 96, 9027
Law C. J. et al., 2021, ApJS, 257, 3
Lei E., Mollière P., 2025, JOSS, 112, 7712
Lewis N. K. et al., 2020, ApJ, 902, L19
Li G., Gordon I. E., Rothman L. S., Tan Y., Hu S.-M., Kassi S., Campargue A., Medvedev E. S., 2015, ApJS, 216, 15
Lienert J. L., Bitsch B., Henning T., 2024, A&A, 691, A72
Lothringer J. D. et al., 2025, AJ, 169, 274
Lueber A., Novais A., Fisher C., Heng K., 2024, A&A, 687, A110
Lustig-Yaeger J. et al., 2023, Nat. Astron., 7, 1317
MacDonald R. J., 2023, J. Open Source Softw., 8, 4873
MacDonald R. J., Madhusudhan N., 2017, MNRAS, 469, 1979
Madhusudhan N., Seager S., 2009, ApJ, 707
Madhusudhan N., Amin M. A., Kennedy G. M., 2014, ApJ, 794, 12
Magic Z., Chiavassa A., Collet R., Asplund M., 2015, A&A, 573, A90
May E. M. et al., 2023, ApJ, 959, L9
McKemmish L. K., Yurchenko S. N., Tennyson J., 2016, MNRAS, 463, 771
McKemmish L. K., Masseron T., Hoeijmakers H. J., Pérez-Mesa V., Grimm S. L., Yurchenko S. N., Tennyson J., 2019, MNRAS, 488, 2836
Meech A. et al., 2025, MNRAS, 539, 1381
Mollière P., Van Boekel R., Bouwman J., Henning T., Lagage P. O., Min M., 2017, A&A, 600, A10
Mollière P., Wardenier J. P., Van Boekel R., Henning T., Molaverdikhani K., Snellen I. A., 2019, A&A, 627, A67
Mollière P. et al., 2022, ApJ, 934, 74
Moran S. E. et al., 2023, ApJ, 948, L11
Morbidelli A. et al., 2016, Icarus, 267, 368
Müller S., Helled R., 2024, ApJ, 967, 7
Nasedkin E., Mollière P., Blain D., 2024, J. Open Source Softw., 9, 5875
Öberg K. I., Murray-Clay R., Bergin E. A., 2011, ApJ, 743, 16
Owen J. E., 2020, MNRAS, 495, 3160
Parmentier V., Fortney J. J., Showman A. P., Morley C., Marley M. S., 2016, ApJ, 828, 22
Parmentier V. et al., 2018, A&A, 617, A110
Patel J. A., Espinoza N., 2022, AJ, 163, 228
Patrascu A. T., Yurchenko S. N., Tennyson J., 2015, MNRAS, 449, 3613
Penzlin A. B. T. et al., 2024, MNRAS, 535, 171
Perrin M. D. et al., 2024, STScI JWST Technical Memorandum. STScI, Baltimore
Pluriel W. et al., 2020, AJ, 160, 112
Polyansky O. L., Kyuberis A. A., Zobov N. F., Tennyson J., Yurchenko S. N., Lodi L., 2018, MNRAS, 480, 2597
Richard C. et al., 2012, J. Quant. Spectrosc. Radiat. Transfer, 113, 1276
Rigby J. et al., 2023, PASP, 135, 048001
Scarsdale N. et al., 2024, AJ, 168, 276
Schlawin E. et al., 2023, PASP, 135, 018001
Schneider A. D., Bitsch B., 2021, A&A, 654, A71
Sicilia D. et al., 2025, A&A, 693, A316
Stassun K. G., Collins K. A., Gaudi B. S., 2017, AJ, 153, 136
Tabernero H. M. et al., 2022, MNRAS, 515, 1247
Wakeford H. R., Sing D. K., 2015, A&A, 573, A122
Yang J., Alday J., Irwin P., 2024, J. Open Source Softw., 9, 6874
Yurchenko S. N., Mellor T. M., Freedman R. S., Tennyson J., 2020, MNRAS, 496, 5282
Yurchenko S. N., Owens A., Kefala K., Tennyson J., 2024, MNRAS, 528, 3719
Zamyatina M. et al., 2024, MNRAS, 529, 1776

APPENDIX A: TRANSMISSION SPECTRUM FROM COMBINED NRS1 AND NRS2 LIGHT-CURVE FIT

To investigate whether any offsets in the transit depth between NRS1 and NRS2 could be caused by differences in system parameters, we conducted a combined white light-curve fit between NRS1 and NRS2. We further refitted the Eureka! $R = 400$ light curves using the system parameters obtained by the combined fit and compared to the transmission spectrum obtained when using individual system parameters. The resulting transmission spectra are shown in Fig. A1.

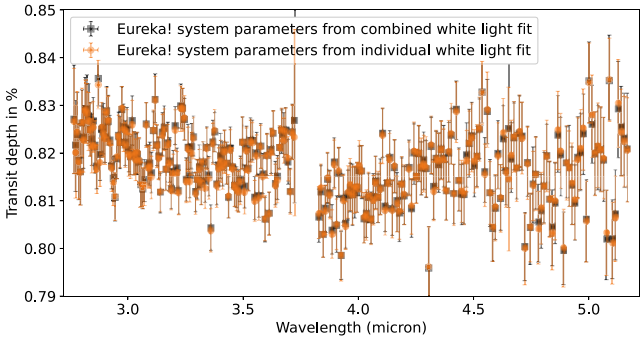


Figure A1. Comparison of two *JWST* NIRSpec/G395H transmission spectrum of KELT-7 b using Eureka! $R = 400$ light curves, one using the system parameters fitted using a combined fit of the two NRS1 and NRS2 white light curves and one using the system parameters individually retrieved from the NRS1 and NRS2 white light curves. The differences between the two are minor, the transit depths when using the combined fit system parameters are on average <1 and <5 ppm lower for NRS1 and NRS2, respectively, compared to the transit depths using individually fit system parameters. For comparison, the average uncertainties on the transit depth in NRS1 (50 ppm) and NRS2 (69 ppm) are around a factor of seven higher and the fitted offset in the retrieval for Eureka! $R = 400$ is of order 50–70 ppm.

Downloaded from https://academic.oup.com/mnras/article/543/3/2442/8255897 by Imperial College London Library user on 04 November 2025

The effects are minor, on average <5 ppm, compared to the offset found by the retrievals of up to 70 ppm.

APPENDIX B: RETRIEVAL PRIOR RANGES

In Tables B1 and B2, we show the prior ranges of the retrieval parameters for pRT, Poseidon, and NemesisPy (for combined *HST* + *JWST*).

Table B1. Parameters and prior ranges for our retrieval of KELT-7 b Poseidon, pRT, and NemesisPy (in continued Table B2). Note that they are all uniform unless stated otherwise. The rightmost column refers to the literature references of the line lists as follows: [1] Polyansky et al. (2018), [2] Yurchenko et al. (2020), [3] Li et al. (2015), [4] Yurchenko et al. (2024), [5] Coles, Yurchenko & Tennyson (2019), [6] Barber et al. (2014), [7] Azzam et al. (2016), [8] Yurchenko et al. (2024), [9] McKemmish et al. (2019), [10] McKemmish, Yurchenko & Tennyson (2016), [11] Patrascu, Yurchenko & Tennyson (2015), [12] Gorman, Yurchenko & Tennyson (2019), [13] John (1988).

	Poseidon Parameter	Prior range	Reference
Equilibrium	C/O	0.2–1.2	
chemistry	log(M/H)	−1–2	
Free chemistry	$\log(H_2O)$	−12–−1	[1]
base species	$\log(CO_2)$	−12–−1	[2]
(VMR)	log(CO)	−12–−1	[3]
	$\log(CH_4)$	−12–−1	[4]
	$\log(NH_3)$	−12–−1	[5]
	log(HCN)	−12–−1	[6]
	$\log(H_2S)$	−12–−1	[7]
Free chemistry	log(SiO)	−12–−1	[8]
high-temperature	log(TiO)	−12–−1	[9]
species	log(VO)	−12–−1	[10]
(VMR)	log(AlO)	−12–−1	[11]
	log(SH)	−12–−1	[12]
Temp. profile	T (K)	400–3000	
Ref. radius	$R_{\rm ref}(R_p)$	0.85–1.15	
Planet gravity	$\log g$	$\mathcal{N}(\log g_p, \log g_{p,err})$	
Clouds	$\log P_{\rm cloud}$(bar)	−7–2	
Offset	$\delta_{\rm rel}$ (ppm)	−1000–1000	
	pRT Parameter	**Prior range**	**Reference**
Equilibrium	C/O	0.1–1.5	
chemistry	log(M/H)	−1–2	
Free chemistry	$\log(H_2O)$	−10–−1e-6	[1]
base species	$\log(CO_2)$	−10–−1e-6	[2]
(mass fractions)	log(CO)	−10–−1e-6	[3]
	$\log(CH_4)$	−10–−1e-6	[4]
	$\log(NH_3)$	−10–−1e-6	[5]
	log(HCN)	−10–−1e-6	[6]
	$\log(H_2S)$	−10–−1e-6	[7]
Free chemistry	log(SiO)	−10–−1e-6	[8]
high-temperature	log(TiO)	−10–−1e-6	[9]
species	log(VO)	−10–−1e-6	[10]
(mass fractions)	log(AlO)	−10–−1e-6	[11]
	log(SH)	−10–−1e-6	[12]
Temp. profile	T (K)	1000–3000	
Ref. radius	$R_{\rm ref}(R_p)$	0.8–1.2	
Planet gravity	$\log g$	$\mathcal{N}(\log g_p, \log g_{p,err})$	
Clouds	$\log P_{\rm cloud}$(bar)	−8–2	
Offset	$\delta_{\rm rel}$(ppm)	−200–200	

Table B2. continued Table B1, for NemesisPy.

	NemesisPy Parameter	Prior range	Reference
Equilibrium	C/O	0.1–3.9	
chemistry	log(M/H)	−4–8	
Free chemistry	$\log(H_2O)$	−12–−0.5	[1]
base species	$\log(CO_2)$	−12–−0.5	[2]
(VMR)	log(CO)	−12–−0.5	[3]
	$\log(CH_4)$	−12–−0.5	[4]
	$\log(NH_3)$	−12–−0.5	[5]
	log(HCN)	−12–−0.5	[6]
	$\log(H_2S)$	−12–−0.5	[7]
Free chemistry	log(SiO)	−12–−0.5	[8]
high-temperature	log(TiO)	−12–−0.5	[9]
species	log(VO)	−12–−0.5	[10]
(VMR)	log(AlO)	−12–−0.5	[11]
	log(SH)	−12–−0.5	[12]
	$\log(H^-)$	−15–−2	[13]
6 parameter T-p	α_1	0.02–2	
	α_2	0.02–2	
	$\log P_1$	−9–2	
	$\log P_2$	−9–2	
	$\log P_3$	−9–2	
	$T_{\rm ref}$	1000–3000	
Ref. radius	$R_{\rm ref}(R_p)$	0.85–1.15	
Ref. pressure	$P_{\rm ref}$ (bar)	−9–2	
Clouds	$\log P_{\rm cloud}$(bar)	−9–2	
	$\log a$	−5–5	
	γ	−10–0	
	$\phi_{\rm cloud}$	0–1	
Offset	$\delta_{\rm rel}$ (ppm)	$\mathcal{N}(0, 500)$	

APPENDIX C: RETRIEVAL RESULTS

In Table C1, we show the retrieved parameter from equilibrium and free chemistry retrievals by pRT and Poseidon using the three reductions and two resolutions of the *JWST* NIRSpec/G395H retrievals transmission of KELT-7 b.

Downloaded from https://academic.oup.com/mnras/article/543/3/2442/8255897 by Imperial College London Library user on 04 November 2025

Table C1. Atmospheric retrieval results: the median values with the uncertainties as 16th and 84th percentiles. Note that the offset in POSEIDON and pRT is defined in the opposite direction, so their signs are opposite.

Input spectrum	$\ln \mathcal{Z}$	$\log_{10} g$ (cgs)	T (K)	$R_{\rm ref}$ ($R_{\rm Jup}$)	$\log P_{\rm cloud}$ (bar)	Offset (ppm)
EUREKA!, $R = 400$						
pRT: equilibrium chemistry	1971.2 ± 0.1	$3.15^{+0.07}_{-0.06}$	1620^{+300}_{-320}	1.55 ± 0.02	$-4.04^{+1.13}_{-0.83}$	-52^{+10}_{-9}
pRT: free chemistry (base)	1966.3 ± 0.1	3.11 ± 0.08	2040^{+560}_{-610}	1.59 ± 0.01	$0.38^{+1.10}_{-1.21}$	-66^{+15}_{13}
POSEIDON: equilibrium chemistry	1972.24 ± 0.11	$3.14^{+0.03}_{-0.03}$	1380 ± 300	$1.54^{+0.01}_{-0.01}$	$-3.32^{+0.94}_{-1.02}$	51^{+10}_{-11}
POSEIDON: free chemistry (base)	1969.14 ± 0.12	$3.13^{+0.03}_{-0.03}$	1680^{+630}_{-1060}	$1.56^{+0.02}_{-0.01}$	$0.63^{+0.90}_{-0.94}$	67^{+11}_{-13}
TIBERIUS, $R = 400$						
pRT: equilibrium chemistry	1979.9 ± 0.1	$3.16^{+0.07}_{-0.08}$	1350^{+370}_{-270}	$1.56^{+0.01}_{-0.02}$	$-3.44^{+1.15}_{-1.24}$	-26 ± 10
pRT: free chemistry (base)	1976.0 ± 0.5	$3.12^{+0.08}_{-0.07}$	1760^{+640}_{-750}	1.57 ± 0.01	$0.31^{+1.13}_{-1.31}$	-38^{+16}_{-13}
POSEIDON: equilibrium chemistry	1980.21 ± 0.11	$3.14^{+0.03}_{-0.03}$	1220^{+290}_{-180}	$1.55^{+0.01}_{-0.02}$	$-2.89^{+0.67}_{-1.01}$	28^{+10}_{-11}
POSEIDON: free chemistry (base)	1977.52 ± 0.13	$3.12^{+0.03}_{-0.03}$	1950^{+510}_{-570}	$1.56^{+0.01}_{-0.01}$	$0.65^{+0.87}_{-0.93}$	42^{+12}_{-12}
EXOTIC-JEDI, $R = 400$						
pRT: equilibrium chemistry	1923.8 ± 0.1	$3.17^{+0.07}_{-0.08}$	1250^{+270}_{-150}	$1.56^{+0.01}_{-0.02}$	$-2.37^{+2.36}_{-1.24}$	53^{+11}_{-10}
pRT: free chemistry (base)	1918.5 ± 0.2	3.14 ± 0.08	1310^{+570}_{-430}	1.57 ± 0.01	$0.30^{+1.14}_{-1.15}$	47^{+19}_{-17}
POSEIDON: equilibrium chemistry	1923.61 ± 0.12	$3.15^{+0.03}_{-0.03}$	1130^{+110}_{-70}	$1.561^{+0.002}_{-0.005}$	$-0.60^{+1.80}_{-1.42}$	-55^{+11}_{-10}
POSEIDON: free chemistry (base)	1920.83 ± 0.12	$3.14^{+0.03}_{-0.03}$	910^{+240}_{-140}	$1.570^{+0.004}_{-0.006}$	$0.41^{+1.04}_{-1.04}$	-60^{+14}_{-13}
EUREKA!, $R = 100$						
pRT: equilibrium chemistry	526.4 ± 0.5	$3.14^{+0.06}_{-0.07}$	1710^{+280}_{-360}	1.55 ± 0.02	$-4.23^{+1.23}_{-0.73}$	-54 ± 9
pRT: free chemistry (base)	520.9 ± 0.1	3.11 ± 0.07	2060^{+560}_{-620}	1.57 ± 0.01	$0.41^{+1.04}_{-1.08}$	-68^{+14}_{-13}
POSEIDON: equilibrium chemistry	525.33 ± 0.11	$3.13^{+0.03}_{-0.03}$	1570^{+380}_{-330}	$1.53^{+0.02}_{-0.02}$	$-3.22^{+0.81}_{-0.96}$	54^{+10}_{-9}
POSEIDON: free chemistry (base)	523.88 ± 0.12	$3.12^{+0.03}_{-0.03}$	2120^{+540}_{-650}	$1.55^{+0.01}_{-0.01}$	$0.61^{+0.91}_{-0.94}$	69^{+12}_{-13}
TIBERIUS, $R = 100$						
pRT: equilibrium chemistry	531.5 ± 0.3	3.16 ± 0.06	1560^{310}_{-330}	1.55 ± 0.02	$-4.10^{+1.40}_{-0.79}$	-28^{+10}_{-9}
pRT: free chemistry (base)	526.0 ± 0.1	$3.13^{+0.07}_{-0.08}$	1870^{+610}_{-770}	1.57 ± 0.01	$0.29^{+1.11}_{-1.33}$	-37^{+20}_{-14}
POSEIDON: equilibrium chemistry	532.33 ± 0.11	$3.13^{+0.03}_{-0.03}$	1430^{+300}_{-270}	$1.54^{+0.01}_{-0.02}$	$-3.31^{+0.89}_{-0.92}$	28^{+10}_{-10}
POSEIDON: free chemistry (base)	529.71 ± 0.12	$3.13^{+0.03}_{-0.03}$	1920^{+550}_{-610}	$1.56^{+0.01}_{-0.01}$	$0.54^{+1.00}_{-1.02}$	38^{+13}_{-12}
EXOTIC-JEDI, $R = 100$						
pRT: equilibrium chemistry	501.0 ± 0.3	3.17 ± 0.07	1420^{+300}_{-270}	1.56 ± 0.02	$-3.03^{+1.73}_{-1.16}$	44^{+11}_{-10}
pRT: free chemistry (base)	495.6 ± 0.1	$3.14^{+0.07}_{-0.08}$	1390^{+740}_{-510}	1.57 ± 0.01	$0.34^{+1.10}_{-1.23}$	39^{+20}_{-17}
POSEIDON: equilibrium chemistry	501.70 ± 0.11	$3.14^{+0.03}_{-0.03}$	1210^{+290}_{-120}	$1.56^{+0.01}_{-0.02}$	$-1.97^{+2.30}_{-0.96}$	-44^{+11}_{-11}
POSEIDON: free chemistry (base)	500.12 ± 0.12	$3.13^{+0.03}_{-0.03}$	1320^{+640}_{-490}	$1.56^{+0.01}_{-0.01}$	$0.49^{+1.01}_{-1.06}$	-43^{+15}_{-17}

Downloaded from https://academic.oup.com/mnras/article/543/3/2442/8255897 by Imperial College London Library user on 04 November 2025

APPENDIX D: POSTERIOR DISTRIBUTIONS

Here, we show additional posterior distributions of our retrievals using the three reductions at $R = 400$. In Fig. D4, we display the equilibrium chemistry corner plot while Fig. D2 shows the free chemistry set-up, both using PRT.

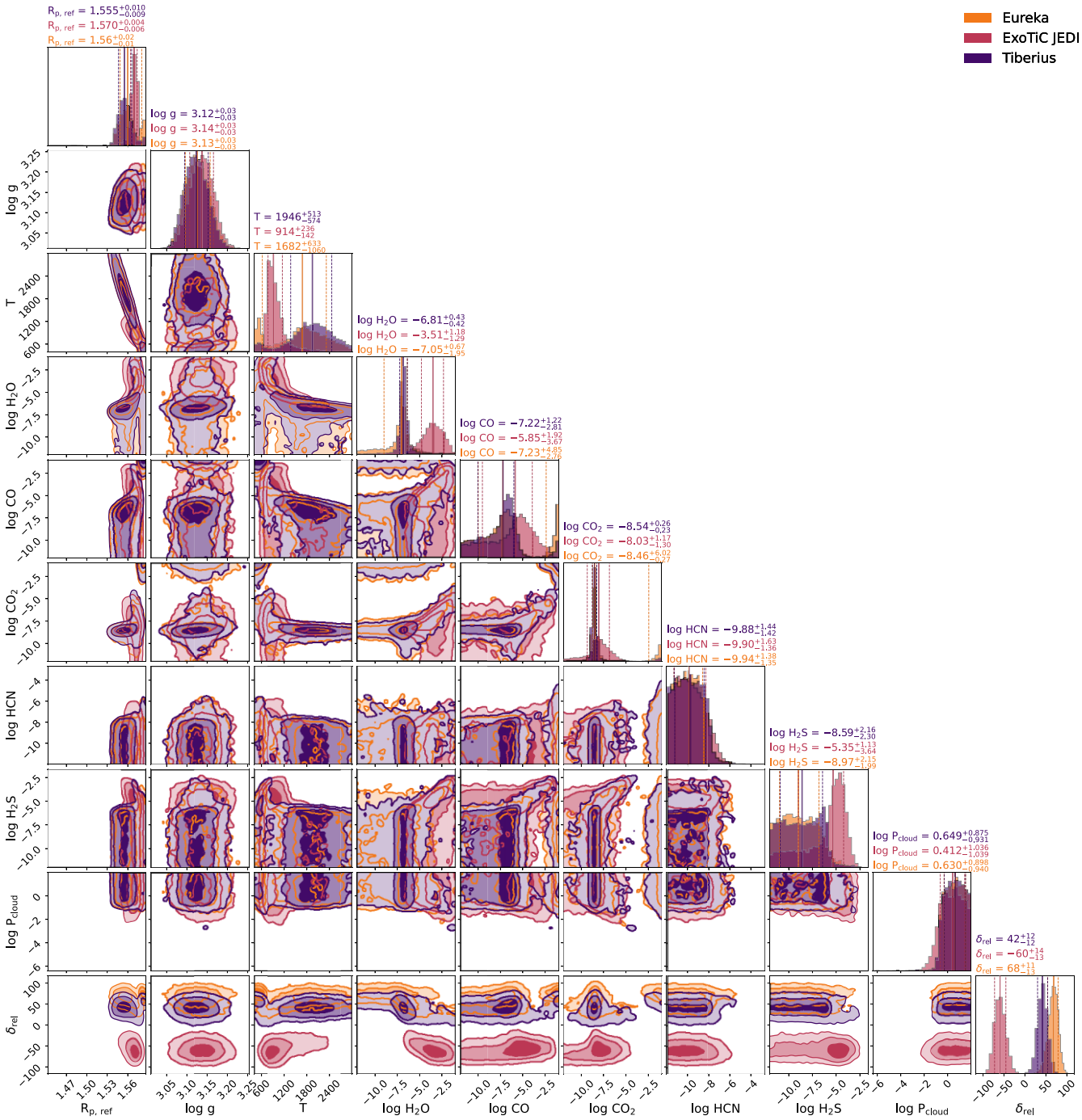


Figure D1. Retrieved posterior distributions using POSEIDON with the free chemistry set-up for the three reductions at $R = 400$.

Downloaded from https://academic.oup.com/mnras/article/543/3/2442/8255897 by Imperial College London Library user on 04 November 2025

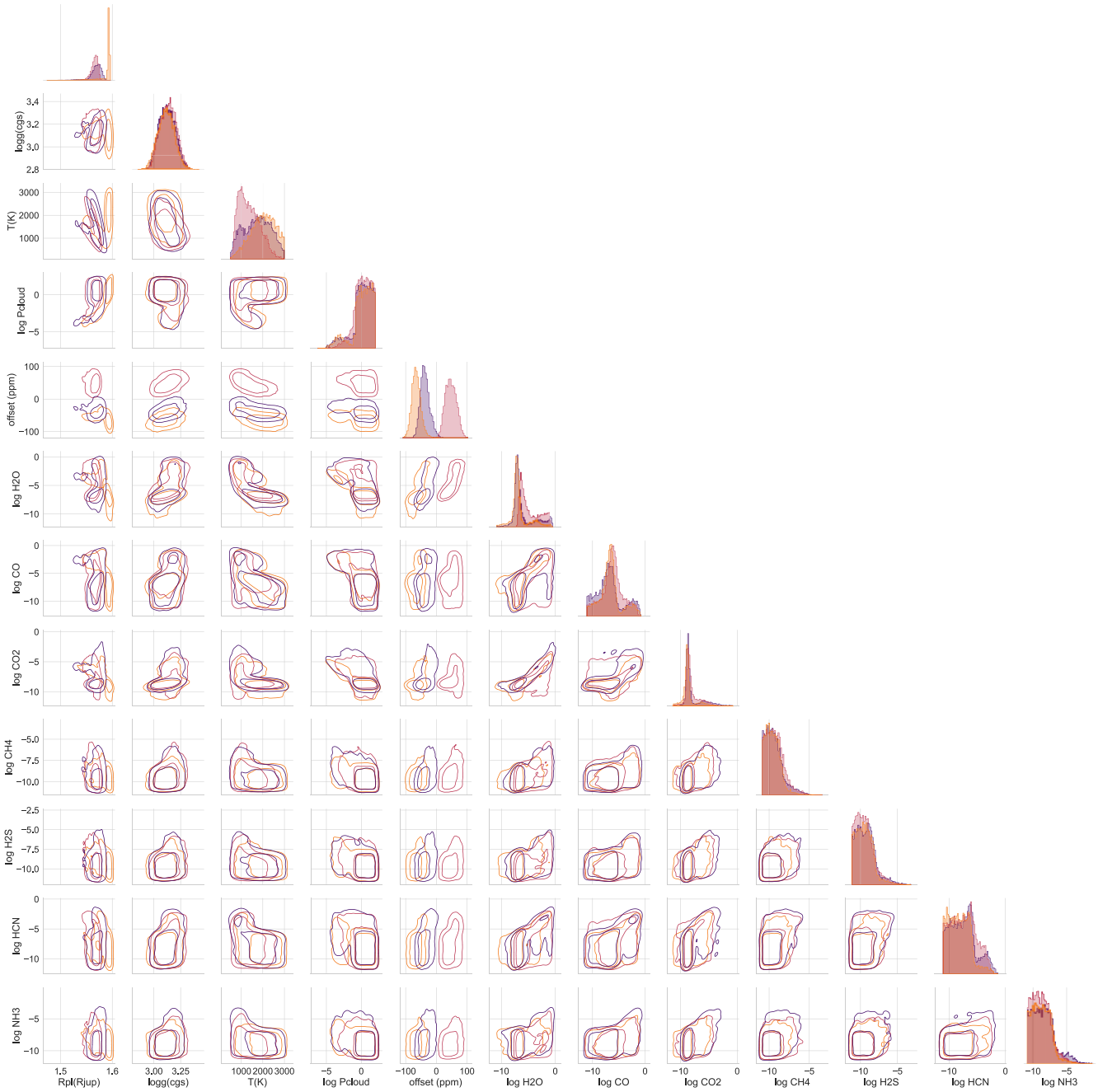


Figure D2. Retrieved posterior distributions using pRT with the free chemistry set-up for the three reductions at $R = 400$.

Downloaded from https://academic.oup.com/mnras/article/543/3/2442/8255897 by Imperial College London Library user on 04 November 2025

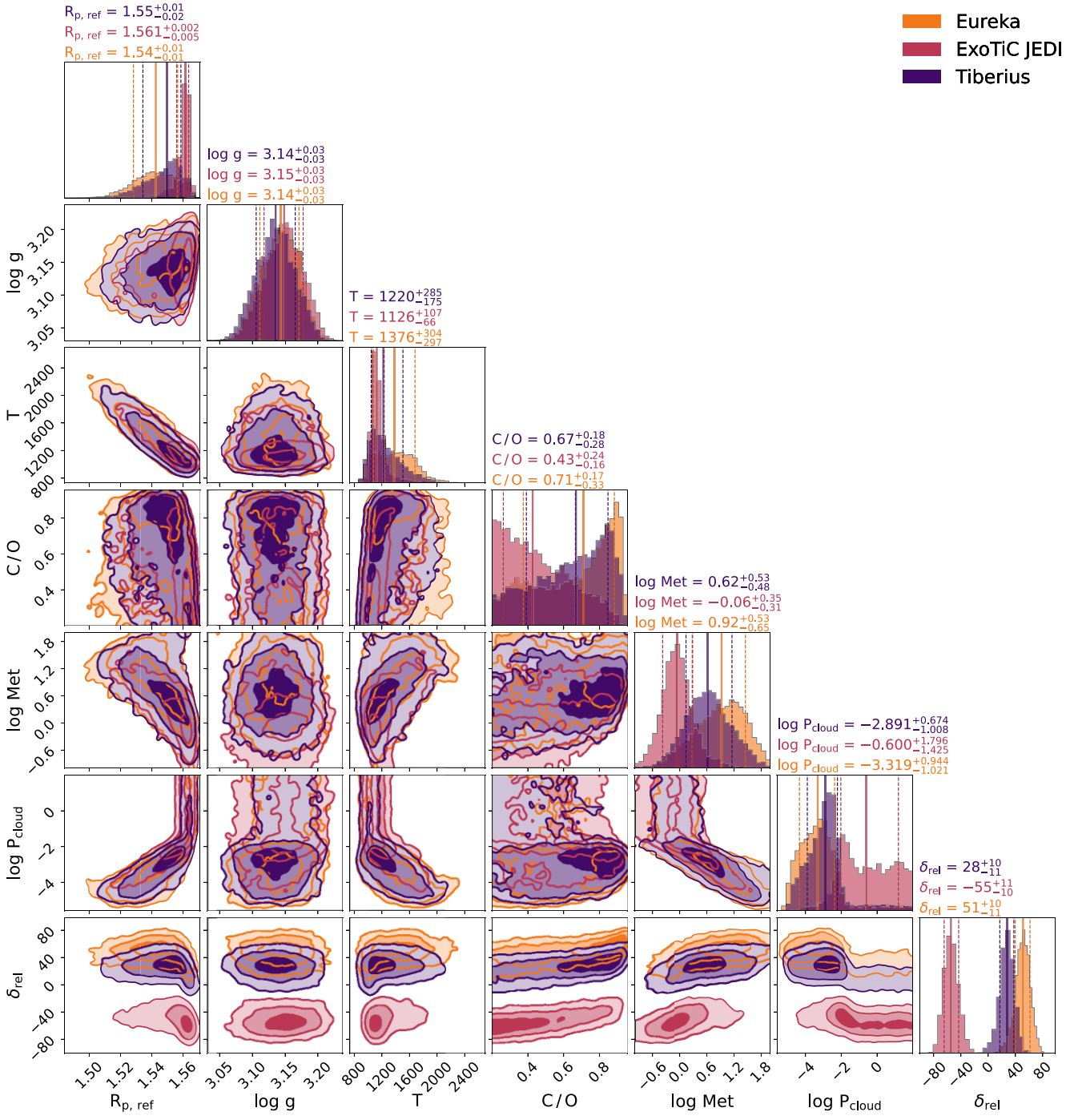


Figure D3. Retrieved posterior distributions using POSEIDON with the equilibrium chemistry set-up for the three reductions at $R = 400$.

Downloaded from https://academic.oup.com/mnras/article/543/3/2442/8255897 by Imperial College London Library user on 04 November 2025

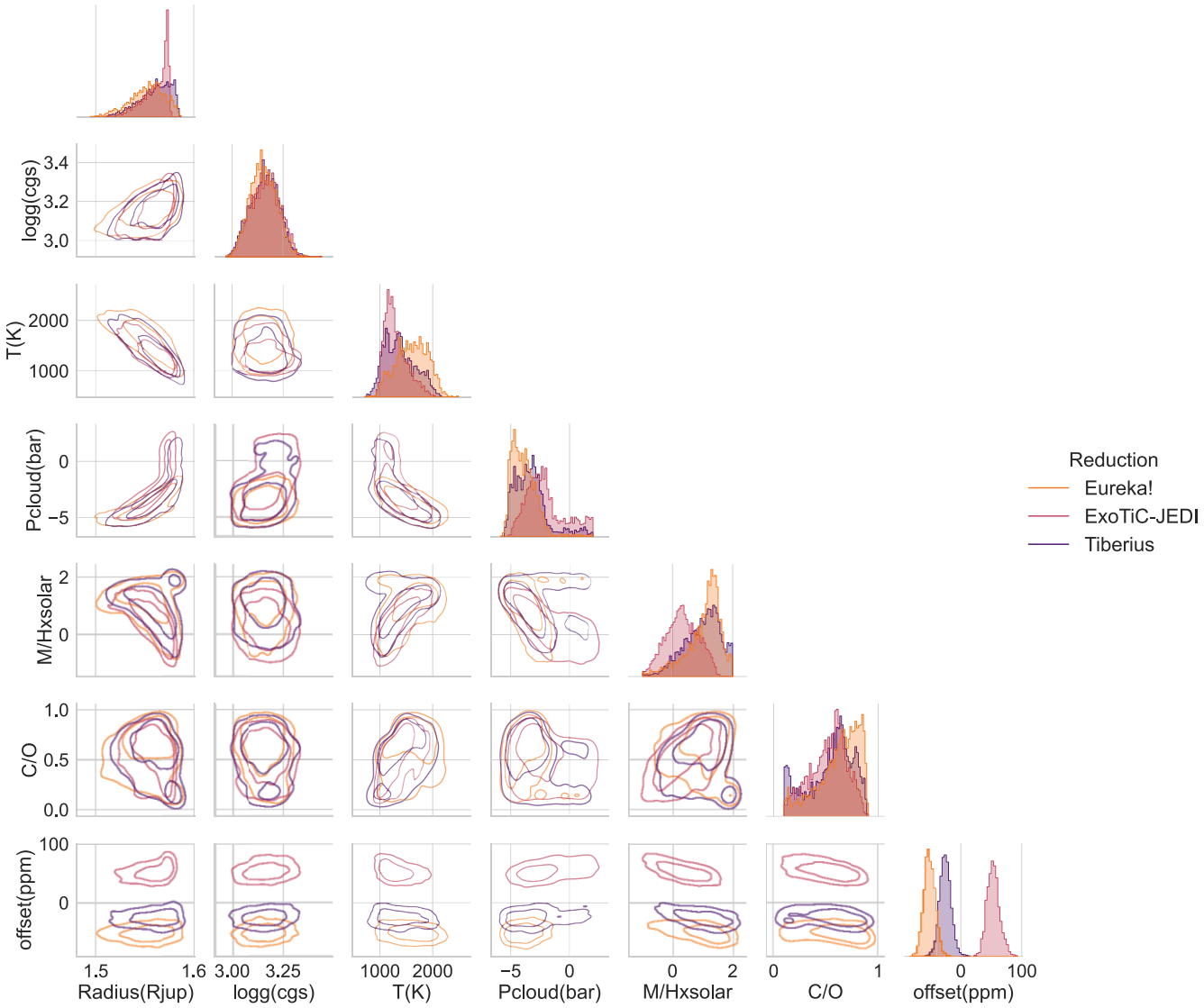


Figure D4. Retrieved posterior distributions using PRT with the equilibrium chemistry set-up for the three reductions at $R = 400$.

Downloaded from https://academic.oup.com/mnras/article/543/3/2442/8255897 by Imperial College London Library user on 04 November 2025

APPENDIX E: COMBINED *JWST* + *HST* EQUILIBRIUM CHEMISTRY RETRIEVAL

Here, we show the NEMESISPY equilibrium chemistry retrieval with free H^- and e^- abundance results when combining our *JWST* NIRSpec/G395H with previously published *HST* transmission spectra of KELT-7 b, Fig. E1.

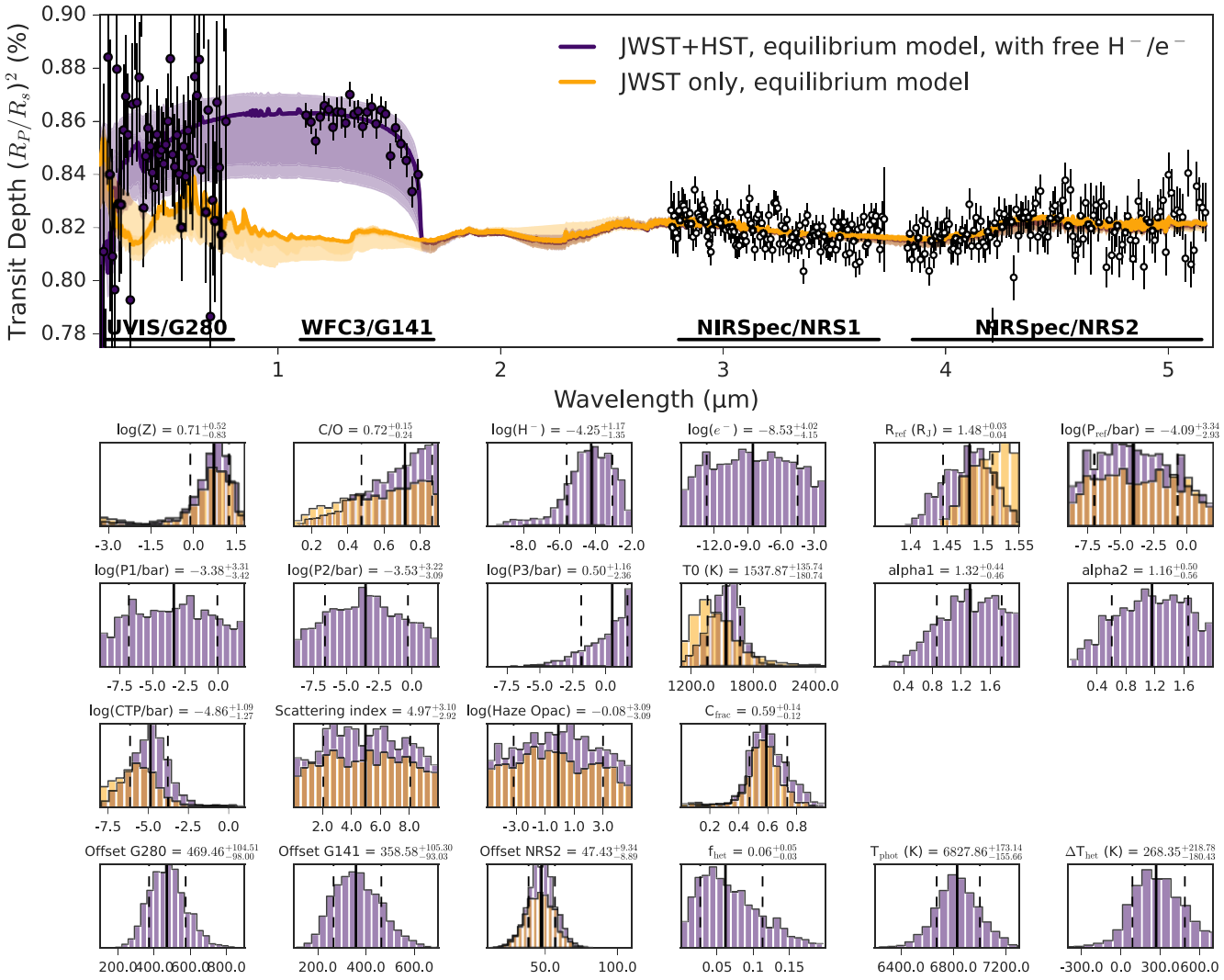


Figure E1. Top: NEMESISPY equilibrium chemistry retrievals comparison between using *JWST* data in combination with previously published *HST* data (dark: including H^- and e^-) and *JWST* data only (light). The colour of the data corresponds to the offset applied from each model. Whilst the retrieval including the *HST* data was conducted with the G280 data set held fixed, here we shift the plot such that the offsets are shown relative to NRS1 to facilitate comparison with Fig. 10. Bottom: The posterior plots for the metallicity and C:O ratio, H^- and e^-, R_{ref} and P_{ref}; temperature (P1, P2, P2, T0, alpha1, alpha2); cloud properties (cloud top pressure, haze scattering index, haze opacity and cloud fraction); offsets; and stellar parameters (heterogeneity fraction, photospheric temperature, heterogeneity temperature relative to photosphere). The colours correspond to the individual models, demonstrating that the inclusion of *HST* data does not provide further constraints for the cloud deck or metallicity. The discrepancy in the retrieved radius is due to the two retrievals referencing the instrument offsets to different baseline instruments (G280 for the full retrieval and NRS1 for the *JWST*-only retrieval). The offsets for both retrievals are presented relative to NRS1 to aid comparison.

This paper has been typeset from a TEX/LATEX file prepared by the author.

© The Author(s) 2025.
Published by Oxford University Press on behalf of The Royal Astronomical Society. This is an Open Access article distributed under the terms of the Creative Commons Attribution License (https://creativecommons.org/licenses/by/4.0/), which permits unrestricted reuse, distribution, and reproduction in any medium, provided the original work is properly cited.

Downloaded from https://academic.oup.com/mnras/article/543/3/2442/8255897 by Imperial College London Library user on 04 November 2025